MASTER

Near-field and far-field optical response of a nanoparticle-on-film system

van Liempt, J.C.

Award date:
2019

Near-field and far-field optical response of a nanoparticle-on-film system

Master Thesis

J.C. van Liempt

Supervisors: dr. R.E. Armstrong & dr. P. Zijlstra

Molecular Biosensing for Medical Diagnostics
Department of Applied Physics
Eindhoven University of Technology

TU/e **EINDHOVEN UNIVERSITY OF TECHNOLOGY**

Abstract

The near-field and far-field optical response of a gold nanoparticle on a gold film have been explored in order to find out how different parameters influence the plasmonic response. Based on this research a design is proposed for a plasmonic biosensor that senses the spacing between the nanoparticle and the film.

In Chapter 5, the effect of particle shape on the heterogeneity in optical response is assessed. Heterogeneities can be greatly reduced by using smooth, monodisperse particles in stead of polydisperse, faceted particles. The relative standard deviation in the measured spectra decreases from 47% for Sigma-Aldrich particles to decreases 31% for nanoComposix particles. Due to the smoothness and high symmetry of the nanoComposix particles, the scattering spectra measurements show a high reproducibility. Residual heterogeneity can be caused by small deviations in particle shapes and sizes, roughness in the particle film, local variations in the refractive index and varying angles of incidence.

When decreasing the gold film thickness a broadening in the longitudinal dipole linewidth is observed while the scattering intensity and resonance wavelength remain constant. Simulations on the near-field show that the near-field enhancement decreases for thinner films. This is due to the decreased dipole moment between a particle and the film when the film thickness is smaller than the skin depth of gold. The tunability of the field enhancement while keeping the resonance wavelength constant can be used in order to study the effect of field-enhancements on fluorescence and SERS. Also the dependency of the optical response of nanoparticles to the spacing from the film is investigated. Nanoparticles are deposited on gold films with spacer layers with varying thicknesses. As the spacing increases from 0 nm to 10 nm a blue-shift in the longitudinal dipole resonance of $\sim$200 nm is observed. In order to propose a suitable film thickness for biosensing, the change in intensity at a probe wavelength as the spacing varies is assessed for varying film thicknesses. Due the narrow linewidth of the longitudinal dipole the 45 nm film shows the largest intensity changes for varying spacings, which makes this the most suitable film thickness for sensing.

Further research is proposed on a better control of the spacer layer thickness, scattering spectra simulations including the wavelength-dependent radiation pattern of the nanoparticle on film, the cause of linewidth broadening with decreasing film thickness, the dielectric functions of gold and chromium films and gold nanoparticles, and increasing the intensity change and the total intensity at a probe wavelength for varying spacings.

Contents

Chapter 1

Introduction

1.1 Point-of-care biosensing

Medical diagnostics relies mainly on testing in a medical laboratory. Sending samples to the laboratory, testing them and returning the results can take hours, up to days, which means that care has to be provided to the patient, without the results of the laboratory testing. In several cases, e.g. acute coronary syndrome and congestive heart failure, a rapid diagnosis (<30 minutes) is needed in order to decide whether a patient is in need of accute care [1]. Testing at the point of care (POC) would allow physicians and other clinical personnel to assess the medical condition of a patient at any desired moment. A comparison of the workflows of medical laboratory testing and POC testing, shows that much time can be saved by testing at the point of care, since POC testing involves less steps and the whole process takes place at one location, Figure 1.1. Several commercial POC sensors are already available, such as HemoCue's hemoglobin test [2] and Roche's International Normalized Ratio (INR) sensor [3], the widely used pregnancy (beta human chorionic gonadotropin detection) and glucose tests are examples of POC tests. A physician can use such a test at a patient's bedside and obtain the results onsite and take immediate action. Another advantage is that these sensors require only a small volume of specimen, e.g. blood or urine [4]. These benefits have led to a growing popularity of POC sensors in hosptials. According to a 2013 report of the Dutch National Institute for Public Health and the Environment, all the surveyed hospitals use some sort of POC biosensor in at least one of their wards, mainly glucose, blood clotting and haemoglobin tests [5].

1.1.1 Continuous monitoring

A POC biosensor enables the detection of concentrations of biomolecules that are implicative of a certain medical condition. A recognition element captures a specific analyte, the molecule to be detected. The biological response is converted into an electrical, optical or chemical signal via a transducer [6]. POC test usually rely upon taking a sample from the blood of urine and testing through the use of a handheld device or a test kit. Intergrating of the sensor into the biological system of interest by

Medical laboratory testing

Doctor's office	**Sampling**	**Transporting**	**Analysis**
Test request →	Phlebotomy →	Samle labeled and transported →	Sample received and prepared
Result received ←		← Reporting of result ←	Analysis
Contact patient for reporting			Validation of result

Point-of-care testing

Decision to test

↓

Sampling (e.g., capillary blood)

↓

Perform test
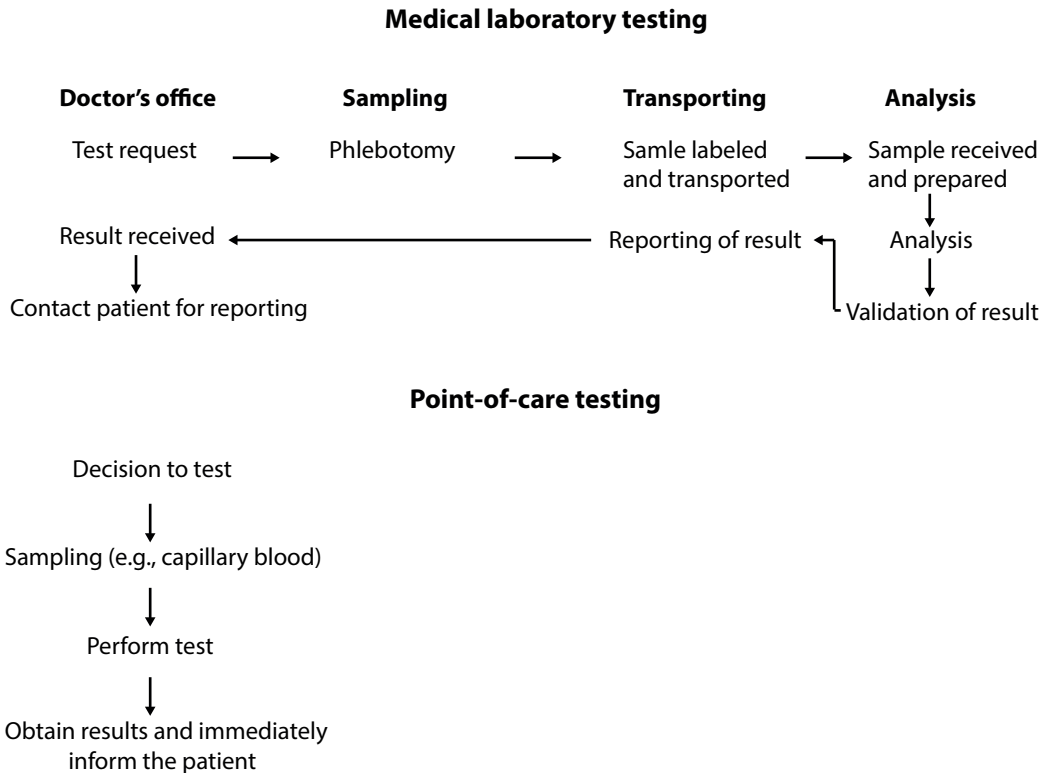
↓

Obtain results and immediately inform the patient

Figure 1.1: Comparison of the workflows of medical laboratory testing and point-of-care testing.

means of e.g. a micro-dialysis probe or catheter, allows the sensor to measure analyte concentrations continuously. The progression of the medical condition of a patient can then be assessed at short time intervals. Within a closed-loop feedback dosing system, such a sensor could be used to precisely adjust the dosage of therapeutic drugs as the medical condition of a patient changes. Continuous monitoring is for example essential in the prevention of hyperglycemia and hypoglycemia. Patients at risk for these conditions are often monitored only four to five times a day, while hourly glucose measurements are required in order to administer the right dosage of insulin in relation to meals, medications, illness, and insulin sensitivity in order to control the concentration of glucose [7].

For this purpose, the continuous POC biosensor has to fulfil some conditions. First, the sensitivity should be tuned so that analytes can be detected at their native concentrations. Depending on the analyte, concentrations in blood can range from millimolar (e.g. glucose [8]) to attomolar (e.g. botulinum toxin type A [9]) concentrations. The concentration of the analyte should fall into the detection range of the sensor. Also the specificity is of importance. The sensor should only report interactions between the target analyte and the recognition element. For this purpose, usually target-specific antibodies or aptamers are used. Also, the interaction between the analyte and recognition element needs to be reversible, so that the sensor can be used multiple times without needing to replace elements of the device. Lastly, the time resolution of the sensor should by high enough to detect analyte concentration changes as fast as possible, so that the clinical personnel can respond to this in time.

1.2 Single-molecule plasmonic nanosensors

Nowadays, POC sensors rely on ensemble measurements. A sample is brought in contact with a sensor surface where analytes can interact with recognition elements. When analytes bind to a recognition elements, the electrical, optical or chemical properties of the sensor surface change. After a certain time the sensor reports the concentration of a certain analyte, based on the change in the electrical, optical or chemical signal. The output will thus give the mean response, meaning that information on single molecules is lost. A sensor should respond to only one type of species. Interactions of other species with the sensor are classified as non-specific. However, in ensemble measurements no distinction can be made between specific and non-specific interactions, since both lead to a changing signal. By sensing the interaction of a single molecule with the sensor, more information can be gained on how a molecule interacts with the sensor, such as the temporal behaviour of the molecule as it is bound to the recognition element. Based on the affinity of the recognition element predictions can be made on how long an analyte will be bound to a recognition element until it unbinds. Deviations in the behaviour of specifically interacting molecules can be recognized as unspecific interactions.

Single-molecule sensing thus allows to specify the interaction of a molecule with the sensor. However, single biological molecules are often hard to measure purely on basis of their intrinsic properties, such as their weight or refractive index, so these molecules often require labels. Labeling the molecules with e.g. fluorescent dyes enables one to detect single molecules. Label-based detection is known to be extremely sensitive [10]. However, labeling the analytes is often cost- and labour-intensive and time-consuming [11].

Plasmon-enhanced detection allows for the detection of non-fluorescent molecules without the need for labeling the analyte [12]. Metallic nanoparticles possess the property of confining visible light to sub-wavelength volumes and thereby enhance the electric field around the particle [13, 14]. The strong electric field around nanoparticles is sensitive to the presence of biomolecules and can thus be used for biosensing [15, 16].

1.2.1 Functionalized nanorods

Single molecule label-free sensing can be achieved by using metallic nanoparticles. Due to the confinement of the electric field around the particle, the particle surface is sensitive to refractive index changes. A localized surface plasmon is excited by exposing the particle to an electric field, such as light. Previously, single molecule label-free sensing using metallic particles has been demonstrated by members of the Molecular Biosensing for Medical Diagnostics group [17, 18] and others [19, 20]. The electric field around the nanoparticle is sensitive to variations in the refractive index, the presence of a molecule will atler the localized surface plasmon resonance (LSPR) and can thus be detected by measuring the nanoparticle's scattering spectrum. The surfaces of the nanoparticles are funcionalized so that analytes can bind to the surface.

When an analyte binds, the local index of refraction changes which translates to a shift in the LSPR, Figure 1.2. A probe wavelength is chosen at which the intensity of the scattered light is assessed. The LSPR shift is however dependent on the molecular weight of the binding molecule i.e. lighter molecules lead to a smaller LSPR shift. The sensitivity is thus limited to weights larger than ~ 50 kDa, in the case of using nanorods [17]. However, several examples can be given of lighter analytes, such as NT- proBNP (17 kDa [21], cystatin-C (13 kDa [22]) and NGAl (25 kDa), which are indicative for cardiac impairment [23], cardiovascular disease [24] and acute kidney injury [25] respectively. In order to detect these, and other lighter analytes, another detection strategy must be developed.
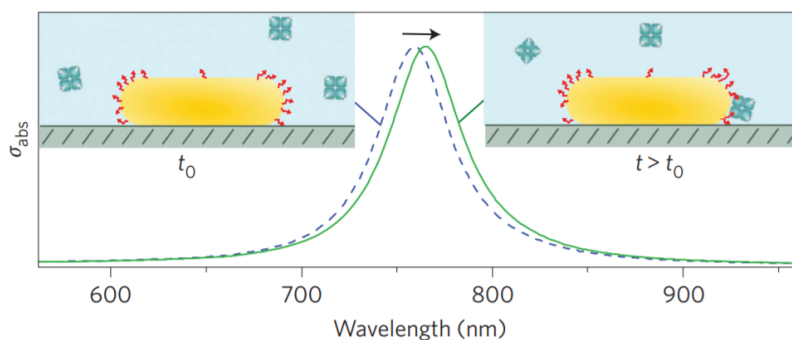
Figure 1.2: A gold nanoparticle is functionalized and immobilized on a glass surface. When an analyte binds to a receptor on the nanorod surface, the spectrum of the nanorod is red-shifted. Source: Zijlstra et al., *Nature nanotechnology*, 2012. [17]

1.2.2 Nanorod-nanosphere geometry

In order to measure molecules lighter than ~ 50 kDa, Visser et al. proposed a sensing strategy where the plasmon shift is independent of the weight of the analyte [26]. A gold nanoparticle with a diameter of 20 nm is tethered to a 20×70 nm gold nanorod via a DNA strand. Due to the localized surface plasmon coupling between the nanorod and the nanoparticle, changing the distance results in a shifting resonance wavelength. The plasmon resonance shift thus depends on the distance between the nanorod and nanoparticle, not on the weight. The scattering intensity of the nanorod-nanoparticle system is probed at one wavelength, Figure 1.3.

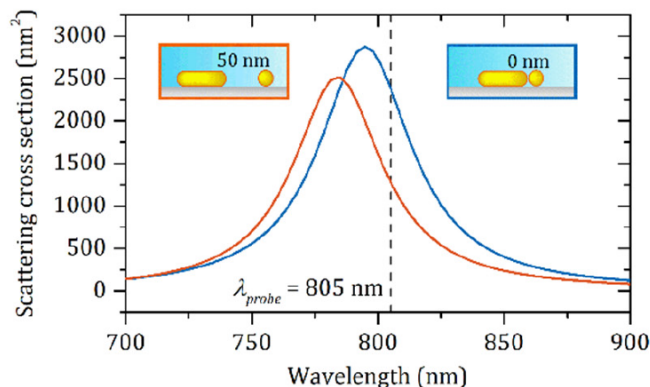Figure 1.3: Scattering spectra of a nanorod and nanoparticle with a 50 nm (red) and a 0 nm (blue) spacing. The scattering intensity is probed at a wavelength of 805 nm. Source: Visser et al., *Nano letters*, 2018. [26]

1.2.3 Nanoparticle-film geometry

Even though the plasmon ruler geometry exhibits large scattering intensity changes upon varying the distance between the nanorod and nanoparticle, the geometry is complex to assemble and therefore not practical. Therefore, a simpler geometry is proposed. A spherical nanoparticle is connected to a gold film via a tether. The LSP in the nanoparticle couples to the delocalized surface plasmon polariton in the film [27]. The coupling between the particle and the film is similar to a particle-particle dimer, that can be excited along the transversal and the longitudinal direction of the dimer [28]. When a nanoparticle is in the vicinity of a metal film, the electric field will be localized in the gap between the particle and the film. The tight confinement leads to a large enhancement of the electric field in the gap region. The theory on plasmonics is further elaborated in Chapter 2. The localization and enhancement of the electric field in the gap between the particle and the film are found to be heavily dependent on the particle-film distance [29–31], the particle size and shape [32–34], the incident angle of excitation [27, 32] and the composition of the nanoparticle and the film [35–37]. The strong field enhancements between the particle and the film and its tunability have been proven to be useful in e.g. measurements on DNA hybridization [38, 39], surface-enhanced Raman spectroscopy (SERS) [40, 41] and the catalysis of electrochemical reactions [40].

The resonance shift induced by varying nanoparticle-film distance could be used to identify the presence of certain analytes. When binding a gold nanoparticle to a gold film via a tether the nanoparticle is restricted in its diffusive motion. The tether can be designed so that it is an aptamer to a certain analyte. As an analyte binds to the tether, the contour length of the tether decreases, leading to a decreased time-averaged distance between the nanoparticle and the film. This results in a red-shift in the LSPR wavelength of the nanoparticle. The intensity at one wavelength could be probed, so that the LSPR shift is indicated by a changing intensity. A change in the time-averaged scattering intensity at the probe wavelength will thus be implicative
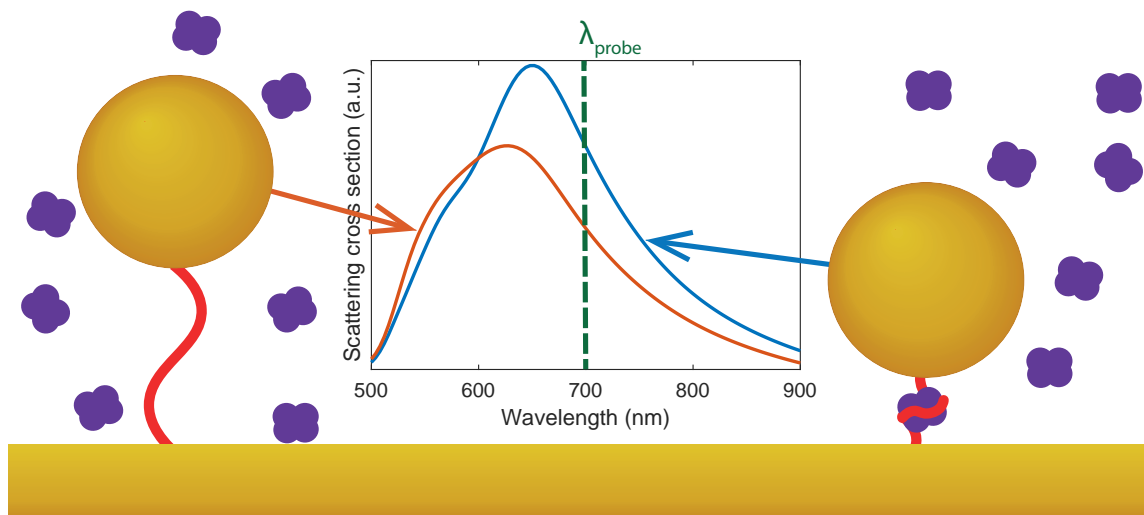
Figure 1.4: The scattering cross section of a gold nanoparticle in the vicinity of a gold film as a function of wavelength before and after an analyte binds to a tether. The change in particle-film distance induces a shift in the LSPR wavelength. λ_{probe} indicates a wavelength at which the intensity change can be probed. The spectra show calculated data for a gold sphere with a diameter of 100 nm separated either 6 nm before binding) or 4 nm (after binding) from a 45 nm gold film.

of an analyte binding to the tether, Figure 1.4. Since the analyte can also unbind, the system is reversible. The weight of the analyte is thus not limiting the sensitivity of the sensor. The sensitivity and reversibility of the system makes it suitable for continuous monitoring.

1.3 Content

In this report the properties of the plasmon resonances of gold nanoparticles on a gold film are investigated, in order to propose a design for the system in Figure 1.4 where the largest intensity changes can be detected as the particle-film distance changes. In Chapter 2 the relevant theory on plasmonics is explained. In the experiments the nanoparticles are deposited directly on the film instead of being tethered. The spectra of nanoparticles on a film are measured using dark-field microscopy. The methods for preparing the samples, conducting the experiments and processing the data are further explained in Chapter 3. In Chapter 4 the results of simulations on the effect of varying several parameters are presented and explained. The heterogeneity in the scattering spectra of the nanoparticles is assessed in Chapter 5, where several contributions to the heterogeneity are elucidated. In Chapter 6, the dependency of the scattering spectra on film thickness and particle-film spacing are investigated, and the near-field behaviour is examined. The spacing between the particles and the film is increased by means of creating polymer layers on the film, before depositing the nanoparticles. Finally, in Chapter 7 the results of Chapter 5, 6 are summarized and ideas for future research are proposed.

Chapter 2

Plasmonics

2.1 Plasma oscillations

Conducting media, such as metals and plasmas, have conduction electrons that can move through the conduction band freely [42]. When such a media is exposed to an external electric field, the conduction electrons will be displaced from their equilibrium. Due to the displacement of these electrons, the opposite charges will exert a restoring force. Therefore, the electrons will collectively oscillate in antiphase with respect to the incident field [43].

The motion of free electrons in an external electric field can be described by

$$\ddot{x} + \gamma \dot{x} = \frac{e}{m_e} E_0 e^{-i\omega t} \tag{2.1}$$

where x is the displacement, γ is the damping term due to scattering events, e is the electron charge, m_e is the electron mass and E_0 and ω are the amplitude and frequency of the external electric field. The dipole moment μ of an electron is obtained by multiplying the electron charge with its displacement: $\mu = ex$. The macroscopic polarization is then given by summing the contributions of all individual electrons: $P = n_e ex$, where n_e is the electron density. The dielectric function can then be calculated using

$$\varepsilon(\omega) = \frac{\varepsilon_0 E_0 + P}{\varepsilon_0 E_0}, \tag{2.2}$$

from which it follows that

$$\varepsilon(\omega) = 1 + \frac{n_e ex}{\varepsilon_0 E_0}. \tag{2.3}$$

Combining equations (2.1) and (2.3) and using the ansatz $x(t) = x_0 e^{-i\omega t}$, one can derive the Drude dielectric function of gold:

$$\varepsilon(\omega) = 1 - \frac{\omega_p^2}{\omega(\omega + i\gamma)} \tag{2.4}$$

with ω_p, the plasma frequency, given by

$$\omega_p = \sqrt{\frac{n_e e^2}{m_e \varepsilon_0}}, \tag{2.5}$$

with n_e the electron density, e the electron charge, m_e the electron mass and ϵ_0 the vacuum permittivity [44]. The electron density is material dependent, while the other parameters are physical constants. The plasma frequency thus depends solely on the material. Note that equation (2.4) gives an approximation of the dielectric function. For simplicity, the contributions of bound electrons. However, in reality bound electrons can be promoted into the conduction band. The real part of the Drude dielectric function corresponds well to measurements on the dielectric function by Johnson & Christy [45] and Palik [46]. The imaginary part, which is related to the refraction of light, of the Drude dielectric function is also in good agreement with measurements for wavelengths longer than 700nm. However, at shorter wavelengths interband transitions will show large contributions to the imaginary part, the damping factor, of the dielectric function.
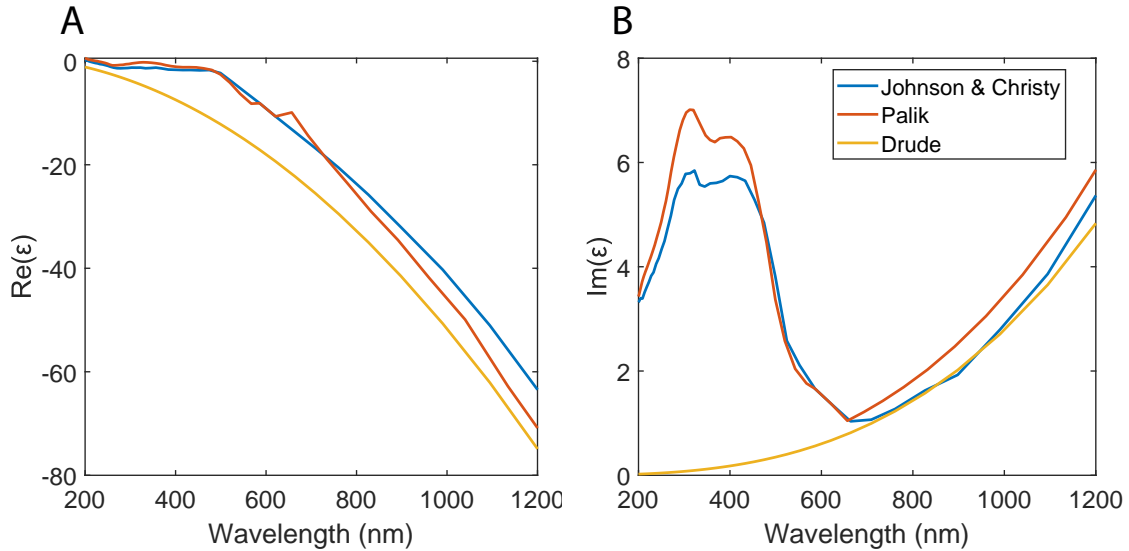

Figure 2.1: (A) Comparison of the real part of measured dielectric function and the Drude dielectric function. (B) Comparison of the imaginary part of measured dielectric function and the Drude dielectric function.

2.2 Localized surface plasmons

Surface plasmons are coherent oscillations of electrons at the interface between two medias with dielectric constants of opposite signs, such as a dielectric and a metal [47]. These surface plasmons can also be localized to subwavelength regions by using, for example, gold nanoparticles [29]. Due to the confinement of the plasmon in a small volume, this is called a localized surface plasmon. When such a nanoparticle is much smaller than the wavelength of the light used to excite the plasmon, the dipole approximation holds, meaning the electric field within the particle is approximately

homogenous and the free electrons in the nanoparticle will all move in phase [48], Figure 2.2A. The electric field is then localized around the nanoparticle, which leads to an enhancement of the electric field Figure 2.2B. Part of the regions were the electric field created by the particle is opposite to that of the light, Figure 2.2C. leading to destructive interference between the two fields and thus absorption of the incoming field. For other regions the constructive interference results in a net field propagating in other directions, and thus induces light scattering [49]. Since the field induced by the nanoparticle spans a region larger than the nanoparticle volume, the scattering cross-section and absorption cross-section are larger than the geometrical cross-section.
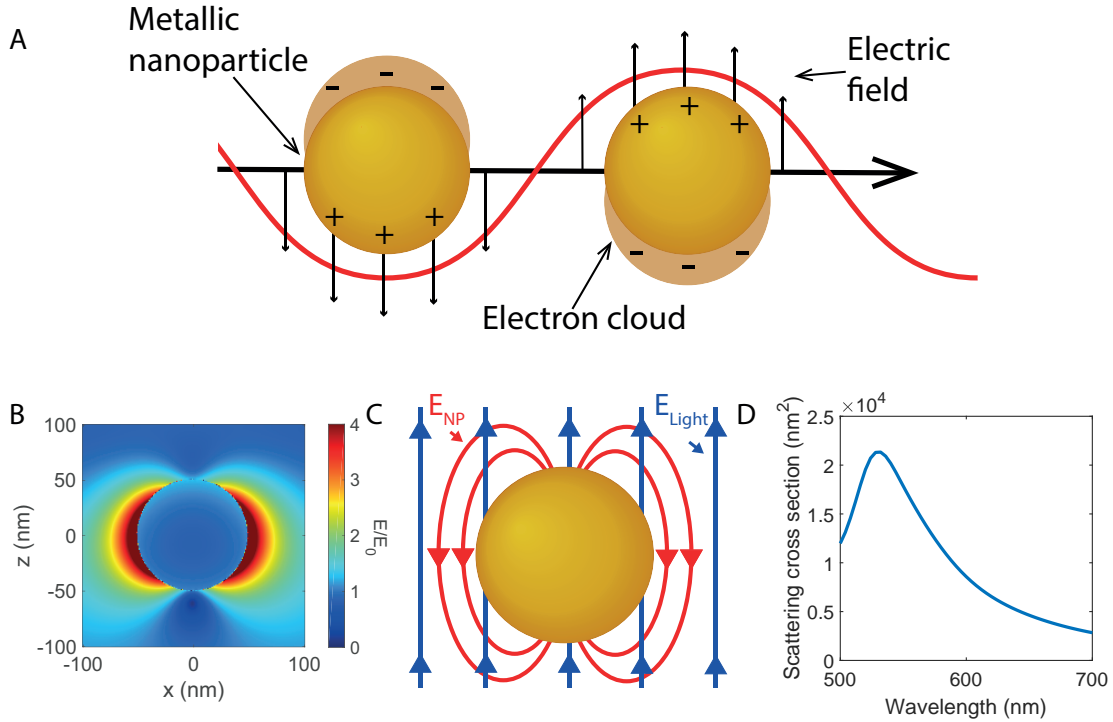

Figure 2.2: (A) Depiction of metal nanoparticles exposed to an electric field. The electron cloud moves in antiphase with respect to the electric field. (B) Boundary element method simulation of the electric field enhancement around a gold nanosphere in air. The diameter of the sphere is 100 nm and the wavelength of the incident light is 550 nm. Boundary element method simulations will be explaied in Chapter 4. (C) Nanoparticle with its localized electric field (red) and an incident external electric field (blue) (D) Boundary element method simulation of the scattering cross-section of a 100nm gold nanoparticle as a function of wavelength, showing the plasmon resonance.

Since the particle is much smaller than the wavelength of light, it can be treated as a dipole, with a dipole moment given by

$$p(\omega) = 4\pi\varepsilon_0\alpha(\omega)E, \qquad (2.6)$$

where E is the external electric field. The polarizability α is given by the Clausius-

Mossotti relation:

$$\alpha(\omega) = 3V \frac{\varepsilon_m(\omega) - \varepsilon_d}{\varepsilon_m(\omega) + 2\varepsilon_d}, \tag{2.7}$$

where $\varepsilon_m(\omega)$ is the frequency-dependent permittivity of the metallic nanoparticle, ε_d is the constant permittivity of the surrounding dielectric and V is the nanoparticle volume. The polarizability exhibits a maximum when

$$\varepsilon_m(\omega) + 2\varepsilon_d = 0, \tag{2.8}$$

meaning that the conduction electrons in the nanoparticle thus form a dipole at the frequency where $\varepsilon_m(\omega) = -2\varepsilon_d$ [50].

Equations (2.4) and (2.8) are combined and γ is set to 0 for simplicity. This gives an approximation for the LSPR frequency:

$$\omega_{LSP} \approx \sqrt{\frac{\omega_p^2}{2\varepsilon_d + 1}}, \tag{2.9}$$

where ω_p is given by equation (2.5). The LSPR thus not only depends on the material of the particle, but also on the surrounding medium. The LSPR can be observed as a peak in the scattering intensity, due to the enhanced scattering cross-section at resonance Figure 2.2D.

2.2.1 Damping of plasmon resonance

Damping of the plasmon resonance leads to a broadening of the linewidth. There are several contributions to the damping:

- Bulk damping due to the absorption of light in gold. This results into intraband excitation within the conduction band and interband exciations which take place between other bands and the conduction band. These effects are described by the imaginary part of the dielectric function, Figure 2.1. From the dielectric functions of gold, one can derive that interband transitions become significant at wavelengths shorter than 600 nm, since here the Drude dielectric function, that does not take into account absorption, starts to deviate from measured dielectric functions.

- Radiation damping, due to the emission of photons by oscillating electrons, by converting kinetic energy into electromagnetic energy. The electrons thus lose energy, resulting in a damping of their motion. This radiation damping rate is linearly proportional to the amount of oscillating electrons and thus larger particles exhibit a larger linewidth broadening due to radiation damping [51].

- Electron-surface scattering, meaning that electrons can scatter at the surface of the nanoparticle and thereby lose energy which also broadens the plasmon resonance. This effect is mainly contributing to the broadening for particles

with a diameter smaller than ~40nm, because 40nm is the electron mean free path in gold [52, 53].

- Electron-defect scattering, meaning that electrons can scatter at defects in the lattice of the metal.

2.2.2 Driven damped harmonic oscillator

An intuitive way of understanding localized surface plasmons is by describing them as harmonic oscillators which are driven by the incident electric field. As the electron cloud is displaced from the equilibrium, it experiences a restoring force $F = -kx$, so its equation of motion is given by

$$m\ddot{x} = -kx \tag{2.10}$$

with k the spring constant and x the displacement. The displacement as a function of time is then

$$x(t) = A\cos(\omega t + \phi) \tag{2.11}$$

with A the amplitude, ω the resonance frequency and ϕ the phase of the oscillation, where

$$\omega_0 = \sqrt{k/m}, \tag{2.12}$$

with m the mass of the electron cloud. However, taking into account the driving force and damping terms alters the equation of motion. A driven damped oscillator is described by

$$m\ddot{x} = -kx - m\beta\dot{x} + F_{ex}. \tag{2.13}$$

The $-kx$ term is recognized as the restoring force (equation (2.10)), $-m\beta\dot{x}$ represents the damping, with β the damping constant and F_{ex} is the driving force. In the absence of a driving force, this equation can be solved by assuming

$$x(t) = ae^{-\gamma t}\cos(\Omega t). \tag{2.14}$$

The solution is then given by

$$x(t) = ae^{-t/\tau}\cos(\Omega t), \tag{2.15}$$

where a is the amplitude, $\tau = 2/\beta$, and $\Omega = (\omega_0^2 - \beta^2/4)^{1/2}$. Due to the damping, the oscillator frequency is thus reduced from ω_0 to Ω and the amplitude exponentially decreases in time at the rate $1/\tau$. Including the contribution of the external driving field does not alter the transient behaviour, but adds a steady-state solution to equation (2.15). The transient behaviour of a driven damped harmonic oscillator is shown in Figure 2.3.
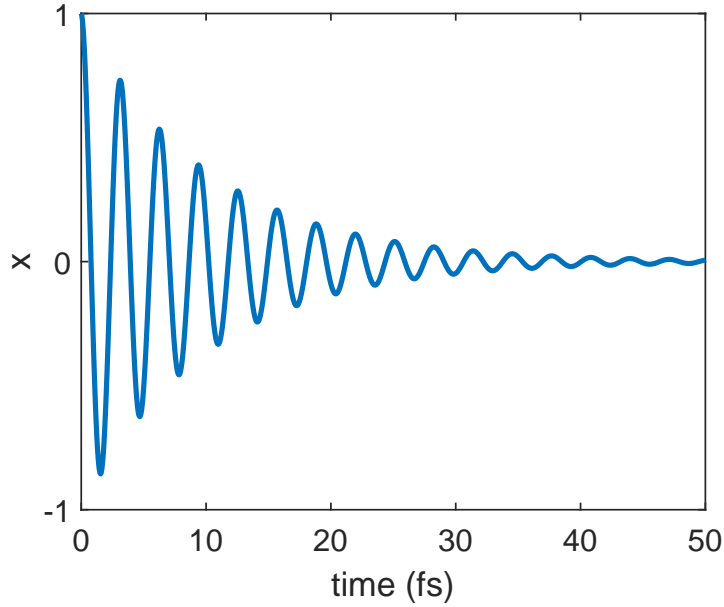
Figure 2.3: Transient behaviour of a driven damped harmonic oscillator.

2.3 Near-field and far-field of a dipole

The near-field and far-field are regions of electromagnetic field around the nanoparticle. Close to the nanoparticle surface, within a distance $r < \lambda$, the non-radiative near-field dominates, while far from the surface, $r > 2\lambda$, the radiating far-field dominates. The transition zone in between is referred to as the intermediate region [54].

The peak intensity can be derived from the equation of motion of a driven damped harmonic oscillator, equation (2.13). Consider that the driving force is given by $F_{ex} = F_0 \cos(\omega t)$. In steady state the motion is then given by

$$x(t) = A(\omega) \cos(\omega t - \phi), \tag{2.16}$$

with an amplitude

$$A(\omega) = \frac{F_0/m}{\sqrt{(\omega_0^2 - \omega^2)^2 + (\beta\omega)^2}}, \tag{2.17}$$

with ω_0 the resonance frequency given by equation (2.12). From equation (2.17) it follows that the amplitude is largest at a frequency of

$$\omega_{NF} = \sqrt{\omega_0^2 - \beta^2/2}, \tag{2.18}$$

which is thus red-shifted from the natural frequency ω_0 due to damping of the oscillation.

The fields radiated by a dipole in the radial (r), polar (θ) and azimuthal (ϕ) directions are given by

$$E_r = \frac{\cos(\theta)}{4\pi\varepsilon_0\varepsilon}\left(\frac{2}{r^3} + \frac{n}{c}\frac{2}{r^2}\frac{d}{dt}\right)|\boldsymbol{\mu}(t - nr/c)|, \tag{2.19}$$

$$E_\theta = \frac{\sin(\theta)}{4\pi\varepsilon_0\varepsilon}\left(\frac{1}{r^3} + \frac{n}{c}\frac{1}{r^2} + \frac{n^2}{c^2}\frac{1}{r}\frac{d^2}{dt^2}\right)|\boldsymbol{\mu}(t - nr/c)|, \tag{2.20}$$

$$E_{phi} = 0, \tag{2.21}$$

derivation given in A. In the near-field r^{-3} terms dominate, in the far-field the r^{-1} terms and in the intermediate field the r^{-2} terms. The near-field is thus generated by the displacement of conduction electrons and therefore related to the amplitude of the plasma oscillations and thus the intensity of the near-field should peak at ω_{NF}.

According to equation (2.20), the far-field scattering of a nanoparticle results from the acceleration of the conducting electrons, derivation in Appendix A, so the maximum scattering cross-section should be situated at a similar frequency as the kinetic energy. The kinetic energy can be calculated using

$$T = 1/2m\dot{x}^2, \tag{2.22}$$

where $\dot{x}$ can be derived from equation (2.16). The time average of the kinetic energy is then given by

$$<T> = \frac{F_0^2}{4m}\frac{\omega^2}{(\omega_0 - \omega)^2 + (\beta\omega)^2}, \tag{2.23}$$

which peaks at ω_0. Therefore, the far-field scattering cross-section will peak at ω_0. The near-field enhancement peak is thus red-shifted with respect to the maximum scattering intensity in the far-field.

This behaviour is illustrated in Figure 6.7. As the damping constant increases the maximum of the amplitude shifts to lower frequencies while the maximum of the time-averaged kinetic energy remains constant for increasing β.
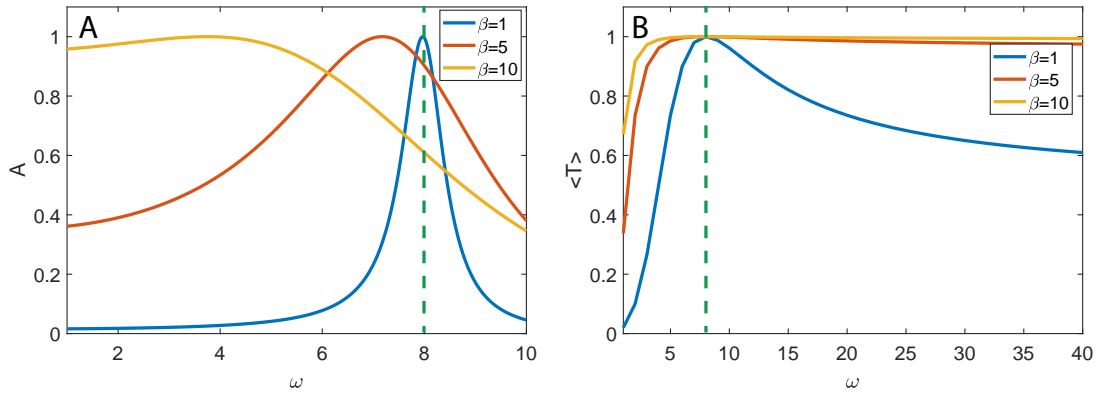
Figure 2.4: Calculations on (A) the amplitude of the steady-state motion and (B) the time averaged kinetic energy for varying values of the damping constant β with a resonance frequency $\omega_0 = 8$, indicated by the green, dashed lines.

2.4 Nanoparticle on film

The largest field enhancements can be found in the most tightly confined fields, such as around sharp corners [55], in the region between two nanoparticles [56], or in the gap between a metallic film and a nanoparticle, which is spaced a few nanometers from the film [57]. When a nanoparticle is in the proximity of a metallic film, Figure 2.5 A, the localized surface plasmon of the nanoparticle couples with the delocalized surface plasmon polariton in the film. When a charge is at a distance d from an infinite conducting plane, it will interact with the film as if there is an opposite charge present in the film also at a distance d from the surface. The plasmon coupling between a nanoparticle and a metallic film can thus be regarded as a nanoparticle coupling to its image, Figure 2.5B.
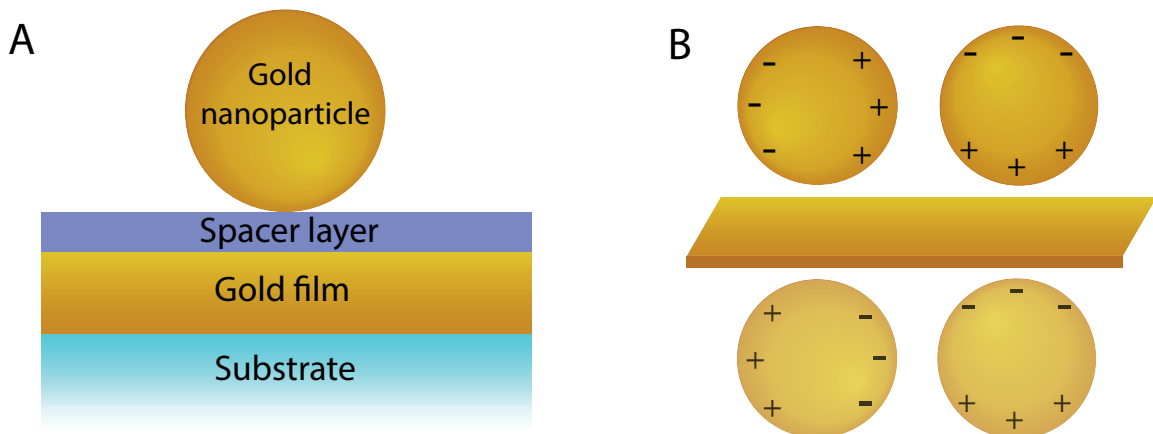

Figure 2.5: (A) Geometry of a nanoparticle on a gold film with a spacer layer. (B) A vertically (left) and horizontally (right) polarized particle and their images in the film (bottom).

14

Due to the reduced symmetry, with respect to a single nanoparticle, the LSP's longitudinal and transversal modes become spectrally distinct [57], where the transversal mode corresponds to the horizontally polarized sphere and the longitudinal mode to the vertically polarized sphere in Figure 2.5B. The oscillation of the conducting electrons in the nanoparticle are influenced by the presence of the gold film. Electrons near the gap between the particle and the film feel the presence of opposite charges in the film. The net charge is therefore reduced and the restoring force between opposite charges in the particle decreases, which thus leads in a red-shift of the resonance frequency. The longitudinal dipole exhibits the largest red-shift in the presence of a film, since the electrons oscillate in the direction normal to the film, so a larger charge accumulation will form at the particle surface in the gap region.

Chapter 3

Materials and Methods

3.1 Sample preparation

Gold films are deposited on glass slides using thermal evaporation. In order to make the gold adhere to the glass surface, a 5 nm chromium layer is deposited on the glass substrate before depositing the gold. The film thicknesses are measured using a Dektak XT Profilometer by blocking gold deposition of a small region with tape and measuring across the edge when the tape was removed, Figure 3.1.

The surface roughness on gold films is best assessed by performing atomic force microscopy (AFM) on the average roughness (R_a) and root-mean-square roughness (R_q) along 50μm lines [58]. These measurements are performed on 10 nm, 15 nm, 30 nm and 45 nm gold films. The results are shown in Appendix B. The values of these parameters were found to be low on all film thicknesses: R_a=0.2-0.4 nm and R_q=0.2-1 nm.

Before depositing gold nanoparticles on the gold film, it is first cleaned in order to remove contaminations. The slide is submerged in a solution of 50 mM KOH and 25% H_2O_2 for five minutes, after which it is thoroughly rinsed with Milli-Q water and dried with N_2.

The nanoparticles that are used in the experiments are nanoComposix ultra uniform 100nm gold nanoparticles, functionalized with PEG12-Carboxyl. The nanoparticle stock solution is diluted with 3 mM NaOH (pH 11-12) to deprotonate the carboxylic acids, induce repulsion, and therefore prevent particle clustering. The gold surface of the slide is coated with particles by spin coating a droplet of 100 μL diluted nanoparticle solution. Afterwards, the slide is cleaned by rinsing it with methanol and dried with N_2.
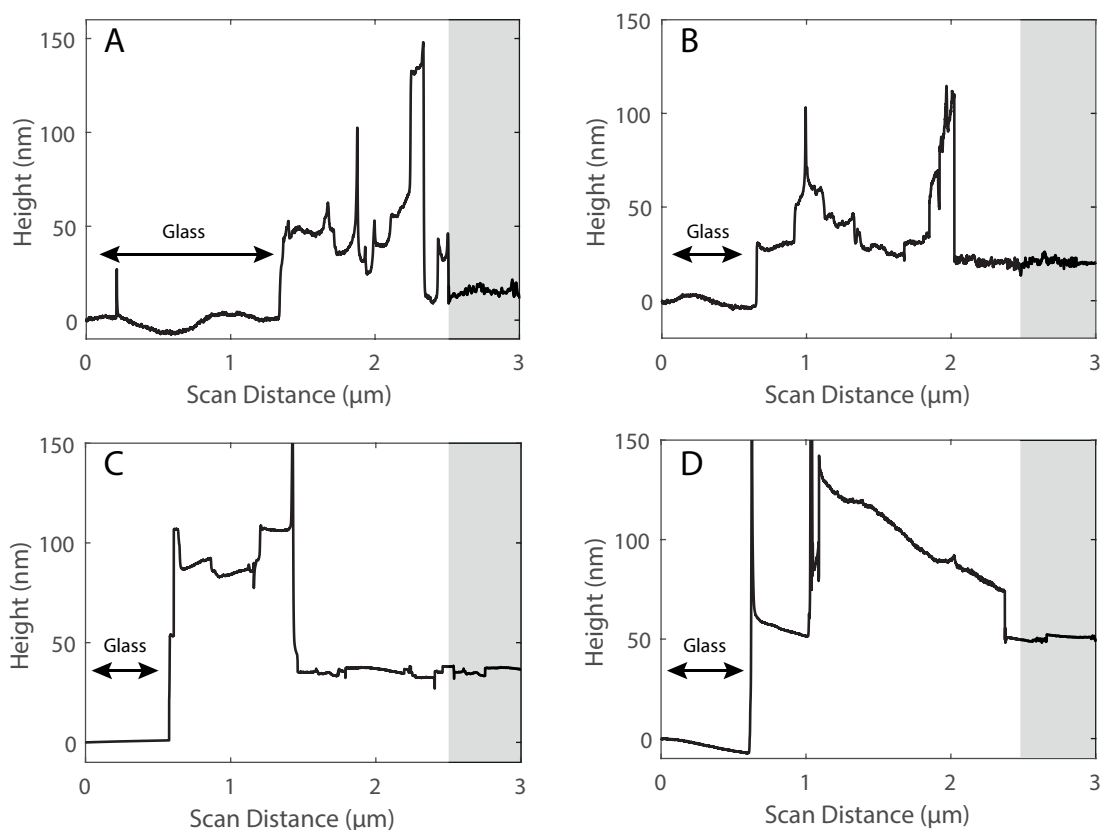
Figure 3.1: (A-D) Height profiles across a region transitioning from bare glass to a 5nm Cr layer plus gold layers of (A) 10nm, (B) 15nm, (C) 30nm and (D) 45nm. The glass region was blocked by tape during the gold evaporation and removed afterwards to analyze the height profile of the gold layer. The measured section was selected by aligning the needle by eye in the softwares camera. Then, the film height determination was calculated by the average height across the final 0.5μm of the scan (shaded) to avoid the noisy portions that stem from peeling back the tape.

3.1.1 Spacer layer deposition

In the cases that the particle needs to be located at a certain distance from the gold film, a dielectric spacer layer can be deposited on the film before spin-coating the nanoparticles. This spacer layer is created via layer-by-layer deposition of positively charged poly(diallyldimethylammonium chloride) (PDADMAC) and negatively charged polystyrene sulfonate (PSS). Such a spacer layer is schematically shown in Figure 3.2A together with the structural formulas of PSS and PDADMAC. These polymers are dissolved in 1 M NaCl at a concentration of 10 mg/mL monomer. First a droplet of 150 μL PDADMAC is deposited on the cleaned gold film and incubated in a humid chamber. After 30 minutes of incubation the film is rinsed thoroughly with first 1 M NaCl, then Milli-Q water and then again with 1 M NaCl. The sample is dried with N_2 and the procedure is repeated with PSS. After depositing the desired amount of layers, the nanoparticles are spin-coated on the spacer layer. The thickness of the layers is characterized via ellipsometry. In Figure 3.2(B) the thickness of the

spacer layer as a function of the amount of individual polymer layers is shown.
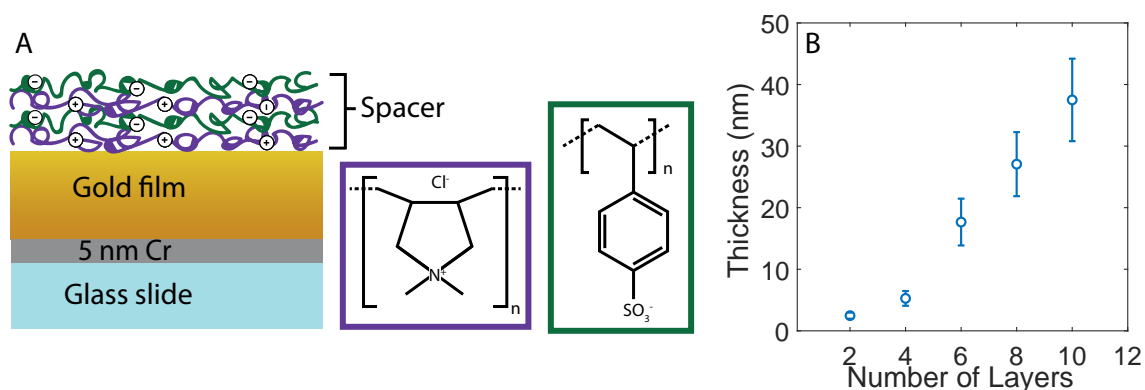

Figure 3.2: (A) PDADMAC (purple) and PSS (green) spacer layer deposited on a gold film. (B) Thickness of the spacer layer as a function of deposited layers. Every two layers consist of one PDADMAC and one PSS layer. The circles indicate the average of three samples, with the errorbars showing the highest and lowest measured values.

3.2 Hyperspectral imaging

The spectra of the nanoparticles are measured using dark-field microscopy, schematically shown in Figure 3.3. The light of a halogen light source is partially blocked by a aperture so that only the outer ring of light will be focused on the sample. Since the numerical aperture of the condenser is larger than that of the objective lens, no direct light will enter the objective lens. Therefore, only the scattered light from the sample is observed.

A sample is illuminated and the scattered light is collected by a 20X Nikon Plan Apochromat objective and then collected by an Andor iXon electron-multiplying charge-coupled device (EM-CCD) camera. The range of numerical apertures (NAs) of the condenser lies between 0.80 and 0.95 and that of the objective is 0.75. The microscope is aligned at the filter where the highest intensity of highest light is observed, in order to prevent saturation of the camera. When aligning the set-up the camera integration time and the opening of the aperture are adjusted so that the background is minimal and the light scattered from the particles is as intense as possible, without saturating the camera.
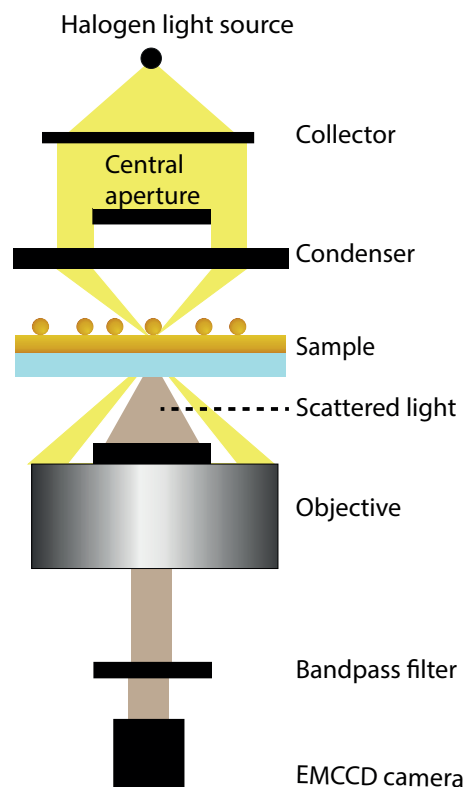

Figure 3.3: Schematic overview of a dark-field microscopy set-up.

In order to measure the spectra of the nanoparticles on a sample, the x- and y-position of the sample is positioned so that at least ∼100 particles are visible in the field of view (400x400µm) and the background is low, typically below 800 counts. Bandpass filters with center wavelengths ranging from 510 nm to 860 nm with a passband of ±5 nm are subsequently placed in front of the camera. At every center wavelength an image of the scattered light is captured and saved. For every filter it is checked whether the microscope is still focused and the z-position of the objective is adjusted if needed.

3.3   Spectral Corrections

The bandpass filters vary in the amount of light that passes through, and the emission intensity of the halogen light source varies by wavelength. Also, sensitivities of the camera and the objective depend on the wavelength of the incoming light, so in order to measure the spectra a correction needs to be applied for external influences to the detected scattering intensity. Therefore, a sample with no nanoparticles on the surface is placed under the microscope. The microscope is defocused so that more light will reach the objective. The procedure of hyperspectral imaging is repeated, except for the refocusing for every filter. The average intensity of the field of view at every wavelength is than calculated and normalized by the average intensity at 510 nm. The result is then shown in Figure 3.4. These values will be used as a correction factor by dividing the collected intensities at all wavelengths by the corresponding spectral correction values.
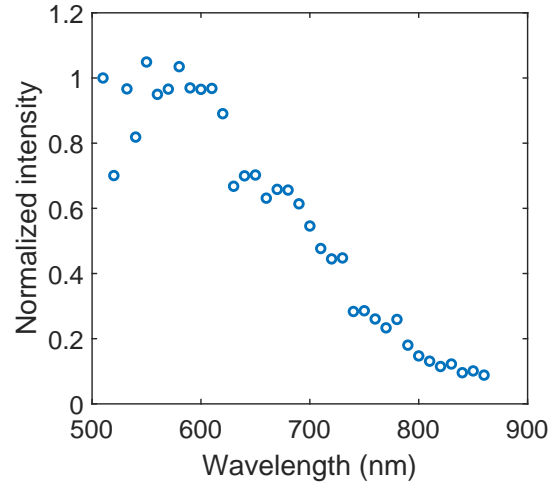
Figure 3.4: Spectral corrections, measured using a slide with a 45 nm gold film. The intensities are normalised to the intensity at 510 nm.

3.4   Data processing

After collecting the images the spectra are calculated in MATLAB using the SPectra4 app, developed by M. Horacek. A region of interest (ROI) of 13×13 pixels is defined around each particle, Figure 3.5. The scattering intensity of a particle is calculated by subtracting the background - the average intensity of the whole field of view - from each pixel in the ROI and subsequently summing the counts of these pixels. This sum is divided by the normalized intensity value (Figure 3.4) of the corresponding

wavelength. This procedure is repeated for the images at the other wavelengths. The resulting spectra of the particles are analysed. Only particles in the center of the field of view are considered, since particles in the periphery tend to be out of focus. The center of the field of view is indicated by the red dashed box in Figure 3.5. Also, spectra that show no plasmon peak, or have to much noise to distinguish a clear plasmon, are discarded. The particles that are located in the center and show a plasmon, are saved and further processed.
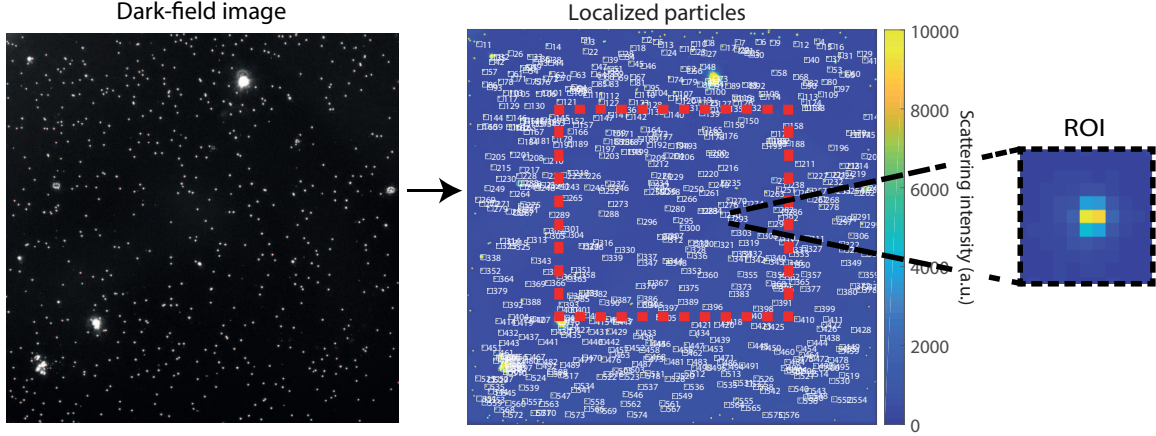

Figure 3.5: The SPectra4 app is used to find the particles in the dark-field image (left) and calculate the spectra. The spectra of the particles in the center of the image (middle, red dashed box) are analysed. A typical ROI of a particle is shown on the right.

The Lorentzian function can be used to fit the plasmon resonance peaks in the measured spectra, which is given by:

$$L(x) = \frac{\frac{1}{2}\Gamma}{(x - x_0)^2 + (\frac{1}{2}\Gamma)^2},\tag{3.1}$$

where Γ is the plasmon linewidth and x_0 the resonance energy. A three-peak Lorentzian function is fitted to the saved spectra. However, not all spectra show three peaks. In order to make a distinction between spectra with three and two peaks, it is assessed whether the fitted peaks show local maxima. If a fit shows indeed three local maxima, so three points that are higher than neighbouring points, there are indeed three distinguishable plasmon resonances. If a fit shows less than three peaks, the spectrum is fitted again, but with a two-peak Lorentzian function, since this will give a more accurate fit. Also, if a three-peak fit shows a peak with a linewidth smaller than 100 meV, a two-peak Lorentzian function is fitted, since this is often a consequence of an incorrect fit. Both the two- and three-peak fitting algorithms are constrained to only assign peaks between wavelengths 500 nm and 900 nm. Examples of a spectra with two peaks and three peaks are shown in Figure 3.6. When further processing the fits, also the fits with a r-squared value lower than 0.85 are discarded, since these are often inaccurate fits.

The Lorentzian fits return the linewidths and the resonance wavelengths of the fitted peaks, which are used to further analyse the spectra.
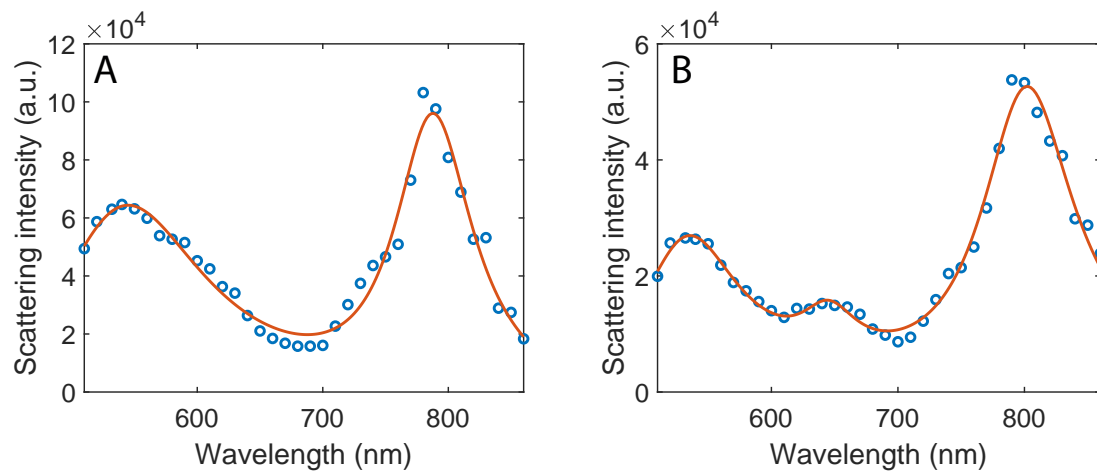

Figure 3.6: Examples of spectra that show two peaks (A) and three peaks (B). The blue circles represent the measured data and the red curve the fit.

Chapter 4

Simulations

4.1 Boundary element method

The simulations are done using a boundary element method approach developed by De Abajo and Howie [59]. The Maxwell equations are solved along the boundaries of all surfaces in order to fulfill a set of boundary conditions. These boundary conditions are defined, based on the dielectric functions of the media. U. Hohenester and A. Trügler developed the metallic nanoparticle BEM (MNPBEM) toolbox to apply this method specifically to metallic nanoparticles [60–62].

The MNPBEM toolbox is used to simulate the optical response of 100 nm gold nanoparticles. The geometry is shown in Figure 4.1, where a nanoparticle is placed on a layer structure consisting of chromium, gold, a dielectric layer and a semi infinite glass slide. The amount of layers and thickness of the layers can be varied. However, the glass layer is present in all simulations. Also, the 5 nm chromium layer is considered in all simulations that include a gold film and is never varied in thickness. The medium surrounding the nanoparticle is air($n = 1$).The refractive index of the spacer layer is set to $n = 1.5$, as Han et al. reported that the refractive index of PDADMAC and PSS multilayers is $\sim$1.52 [63]. The dielectric functions of both gold and chromium are taken from data of Johnson & Christy [45].

Figure 4.1: The geometry that is used in simulations, consisting of a semi-infinite glass substrate, a 5nm chromium layer, a gold film, a spacer layer and a 100nm gold nanoparticle, excited by both p- and s-polarized light equally, under an angle of 70°.

In the simulations, the particles are excited from above by plane waves under an incident angle of 70°. The incident angle follows from the NA of the condenser (0.8-0.95) which means that the angles of the incoming light lie between 53° and 72°. Also, since the incident light is unpolarized, it is assumed that s- and p-polarized light contribute equally, by doing simulations for s-
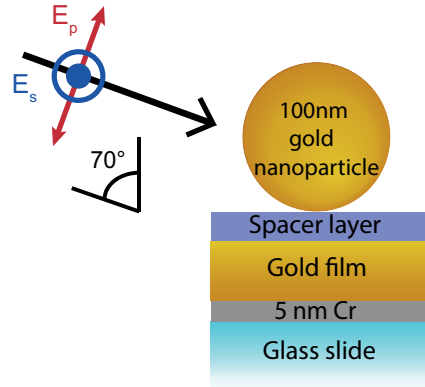
and p-polarized light separately and summing their contributions. The polarization of the incident light is further explained in Section 4.4.

4.2 Mesh size

The mesh size is determined by simulating the spectra of a particle on gold for increasingly finer meshes and thereby find the mesh size for which the values of both the linewidth and resonance wavelength of the longitudinal no longer vary as the mesh size increases. From this calibration, Figure 4.2, it is concluded accurate results can be obtained by simulating spheres with at least 200 vertices.
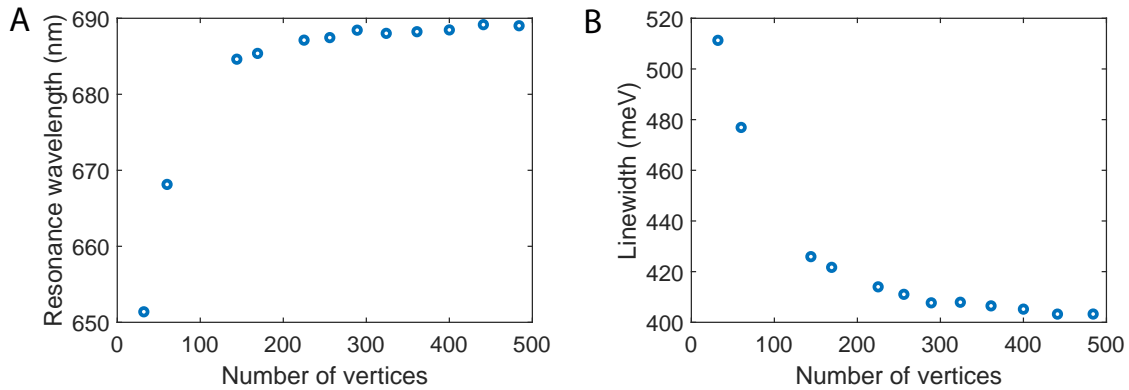

Figure 4.2: (A) The resonance wavelength and (B) the linewidth of the longitudinal dipole mode as a function of vertices in the simulated nanoparticle.

4.3 Plasmonic modes

As explained in Chapter 2, when a nanoparticle couples to a metallic film, the transversal dipole and longitudinal dipole modes become spectrally distinct. Figure 4.3 shows the spectrum for a 100 nm nanoparticle spaced 1 nm away from a 45 nm gold film. Surface charge distributions are calculated to identify the modes corresponding to these peaks. Interestingly, besides the transversal dipole and longitudinal dipole, a quadrupole peak emerges at 540 nm, which is caused by the asymmetry of the particle-on-film system [64].

As stated before, large field enhancements can be found within the gap between a nanoparticle and a metallic film. From Figure 4.3 it becomes clear that for the quadrupole mode and the transversal dipole a 'cold spot' in electric field enhancement can be found at the center of the gap, with the 'hot spots' at the lateral sides of the gap. However, the longitudinal dipole mode exhibits a single 'hot spot' at the gap center. The largest field enhancements can be found in the gap center of the longitudinal dipole due to the charge accumulation at the particle surface in the gap region, which makes the gap region very sensitive to variations in e.g. the refractive index and the nanoparticle geometry.
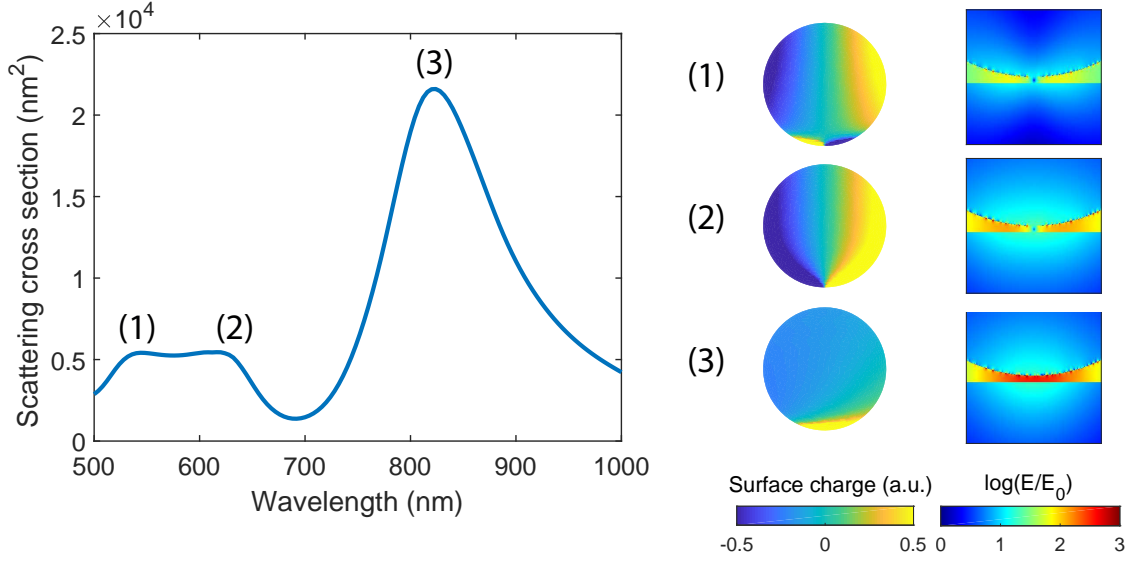
Figure 4.3: Scattering spectrum for a 100 nm particle, on a 45nm thick film with a 1nm spacer. The numbers indicate the (1) quadrupole (2) transversal dipole (3) longitudinal dipole mode. On the right, the corresponding surface charge and near-field plots are shown.

4.4 Polarization

In Figure 4.4A the interaction of a horizontally polarized and a vertically polarized sphere with their images in the film are depicted. The field around the horizontally (left) polarized particle interferes either constructively or destructively with its image in the film, depending on the spacing. The vertically (right) polarized nanoparticle resonantly couples to its image in the film. Whether these modes occur, depends on the polarization of the light. Two different types of polarization of the incident light are defined: p-polarization and s-polarization, with the component of the electric field parallel to the plane of incidence for p-polarized light and perpendicular to the plane of incidence for s-polarized light. When p-polarized light reaches a nanoparticle under a certain incident angle θ, the polarization direction is given by

$$\mathbf{E_p} = \cos(\theta) \cdot E_{0x}\hat{\mathbf{x}} + 0 \cdot E_{0y}\hat{\mathbf{y}} + \sin(\theta) \cdot E_{0z}\hat{\mathbf{z}} \tag{4.1}$$

and for s-polarized light

$$\mathbf{E_s} = 0 \cdot E_{0x}\hat{\mathbf{x}} + 1 \cdot E_{0y}\hat{\mathbf{y}} + 0 \cdot E_{0z}\hat{\mathbf{z}}, \tag{4.2}$$

with the x- and y-directions parallel and the z-direction perpendicular to the film surface. The polarization directions with respect to the film are shown in Figure 4.1. This means that p-polarized light has electric field components in both the horizontal and vertical direction and can therefore excite both the transversal dipole and the longitudinal dipole, Figure 4.4A. S-polarized light however, has only a component in the horizontal direction and thus cannot excite the longitudinal dipole.

24

In Figure 4.4B the scattering spectrum of a particle on film is calculated as a function of the incident angle θ (Figure 4.1) of a superposition of p-polarized and s-polarized light. At an incident angle of 0° both E_p and E_s will only have components in the x- and y-direction. As the incident angle increases, the y-component will remain constant, but the x-component as the z-component increases (equations (4.1) and (4.2)). The simulations in Figure 4.4B confirm this as with increasing incident angle the transversal dipole decreases in intensity while the longitudinal dipole increases.
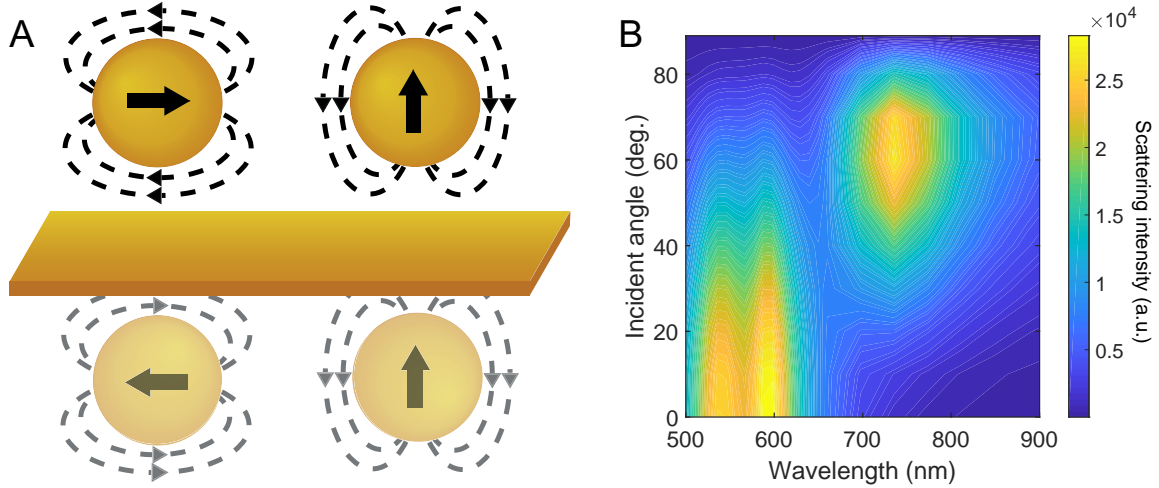

Figure 4.4: (A) Depiction of a transversal dipole (left) and a longitudinal dipole (right) and the electric fields in a nanoparticle, with their images in the film (bottom). (B) Calculated scattering spectra of a 100 nm particle on a 45 nm film with a 1 nm spacing as a function of the incident angle.

4.5 Spacing

4.5.1 Limit

The model solves the system classically using the Maxwell equations, such that non-classical effects are not taken into account. For gaps larger than 1 nm, classical models are sufficient to describe the plasmon response, but they fail to describe the system for smaller gaps [31]. Two effect cause the non-classical behaviour at small spacings (<1nm): quantum tunnelling and electron nonlocality. Due to quantum tunnelling the electromagnetic interactions between the particle and film are reduced, which results in a weakening of the longitudinal dipole mode [65]. Non-locacilty of the electrons means that charges do not reside at the surface, but rather, are spread into the nanoparticle [66]. These effects could thus lead to a reducing intensity of the longitudinal dipole mode and a less pronounced red-shift. It is therefore avoided to simulate spacings smaller than 1nm.

4.5.2 Optical response

In Figure 4.5A the scattering spectra of 100 nm particles on a 45 nm film are shown for varying spacings. As the spacing increases the longitudinal dipole decreases in intensity and blue-shifts. This can be explained intuitively by considering the restoring forces in a particle. When light is incident on a particle, the charges get displaced. Negative and positive charges thus reside on opposite sides of the sphere. This results in a restoring force leading to a resonance condition, as explained in Chapter 2. When the particle is in the vicinity of a gold film, the red-shift in the longitudinal- and transversal dipole mode is due to opposite charges in the particle and film facing each other in the gap region, as depicted in Figure 4.5B. When a particle is placed close to the film surface the net charge is spaced further apart which reduces the restoring force and thus results in a lower resonance frequency. Increasing the distance between the particle and the film diminishes the attractive force between the charges in the particle and the surface, which results in an increasing resonance frequency [67]. Also, the intensity of the longitudinal dipole decreases for increasing spacing, since a stronger electric field will be induced when charges are placed closer together.
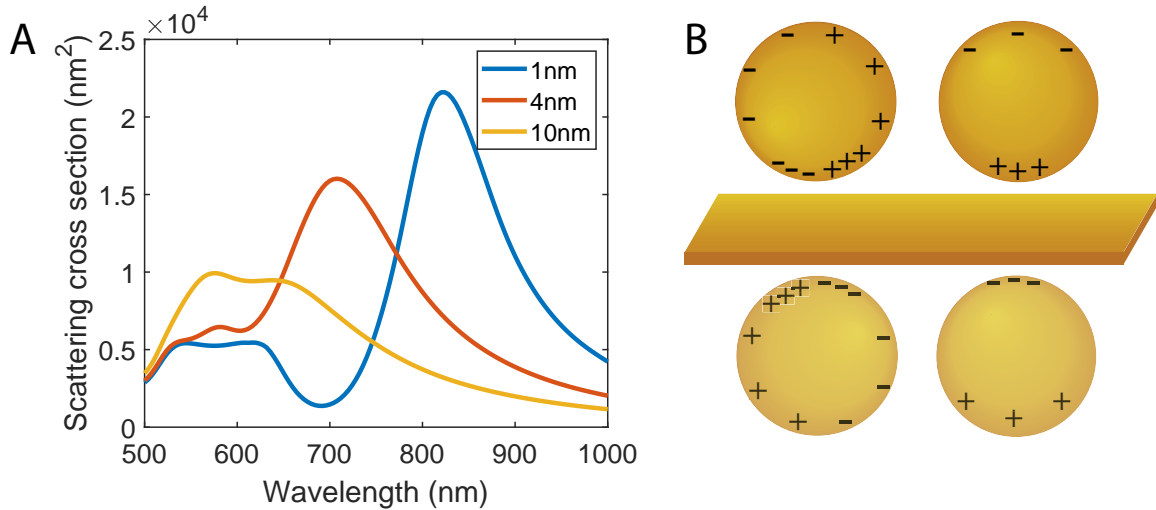
Figure 4.5: (A) Simulated spectra of a nanoparticle on a 45 nm film with a varying spacer layer thickness. (B) A horizontally polarized (left) and a vertically (right) particle with their surface charge distributions and their images in the film (bottom).

4.6 Film thickness

In Figure 4.5A the scattering spectra of 100 nm particles on a film are shown with a 5 nm spacer for varying film thicknesses. When decreasing the film thickness, the resonance wavelength of the longitudinal dipole remains constant while its intensity decreases. Since gold has a skin depth of ∼44nm [68], films exceeding this thickness will act as a mirror where an image charge is formed creating a dipole with the nanoparticle. Decreasing the film thickness to thicknesses below the skin depth will

thus lead to a decrease in the dipole moment [69]. Since the intensity of the radiated light scales quadratically with the dipole moment, equation (2.20), the decreasing film thickness will lead to a decreasing scattering intensity.
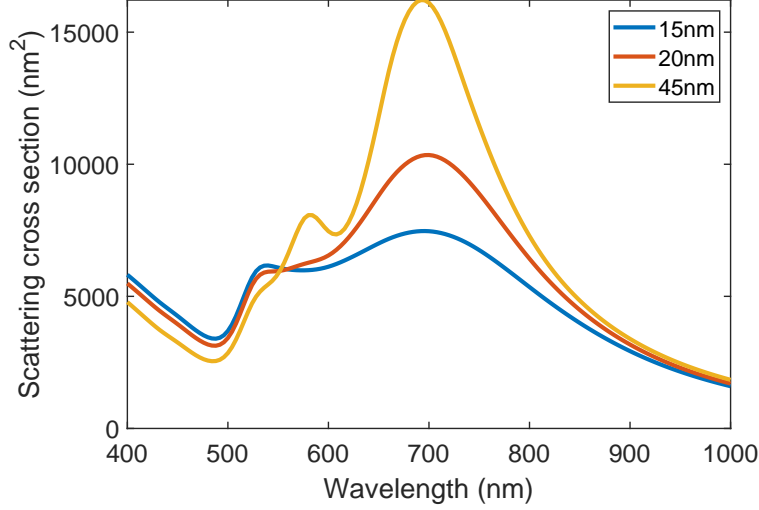

Figure 4.6: Simulated spectra of a 100 nm nanoparticle on a film with a 5 nm spacer layer with a varying film thickness.

4.7 Refractive index of the medium

The refractive index of the medium will have an influence on the plasmon resonance wavelength due to the polarization in the medium. Due to the localized surface plasmon the field around the nanoparticle is greatly enhanced. This influences the polarization of the dielectric medium in this region, which leads to a charge accumulation around the nanoparticle. This partially compensates the charge accumulation of electrons within the nanoparticle. Therefore, the restoring force is reduced and the plasmon resonances will red-shift. The refractive index, n, is related to the polarizability, α, via the Lorentz-Lorenz equation:

$$\frac{n^2 - 1}{n^2 + 2} = \frac{4\pi}{3} N\alpha, \tag{4.3}$$

where N is the number of molecules per volume, meaning that the polarizabilty of the medium increases with increasing refractive index. A medium with a larger refractive index will thus have a larger effect on the plasmon resonances, Figure 4.7. Also, an increasing intensity of the plasmon resonances is observed when increasing the refractive index. This is explained by equation (2.17), where it is found that the amplitude of the electron oscillation at resonance increases as the resonance frequency decreases.
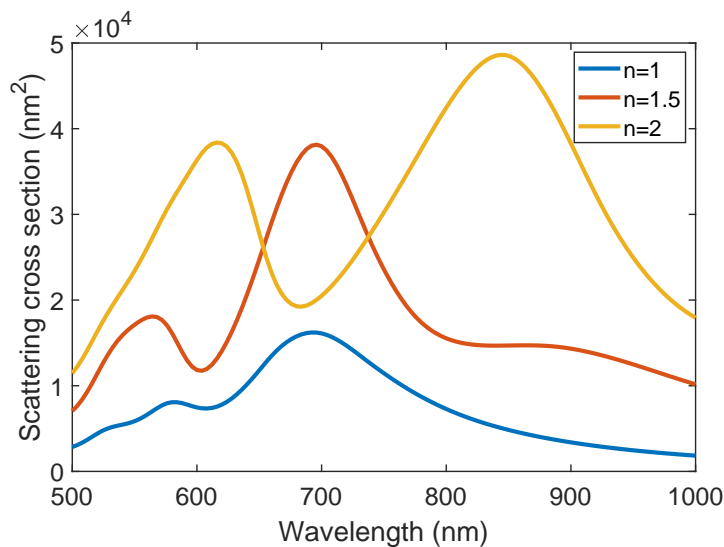
Figure 4.7: Simulated spectra of a 100 nm nanoparticle on a 45 nm film with a 5 nm spacer layer with a varying refractive index of the medium.

4.8   Particle size

The effect of the particle diameter on the scattering spectrum is shown in Figure 4.8. Increasing the particle diameter results in an increasing scattering intensity and a red-shift in the longitudinal dipole resonance wavelength. Due to the larger number of oscillating electrons and therefore a stronger field enhancement. Due to the increased particle size, opposite charges are spaced further apart, Figure 4.5B, such that the restoring force decreases, which thus results in a red-shift of the plasmon resonances.

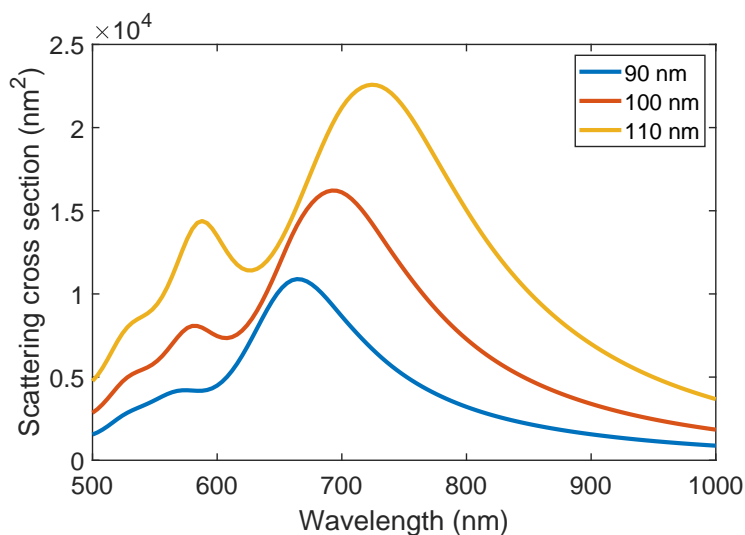
Figure 4.8: Simulated spectra of a nanoparticle on a 45 nm film with a 5 nm spacer layer with a varying particle diameter.

28

Chapter 5

Heterogeneity

Heterogeneity in the far-field optical response of particles on a film can be caused by various factors. In this chapter, the heterogeneity from particle-to-particle and sample-to-sample is assessed and possible causes of the heterogeneity are identified.

The spectra of at least 100 nanoparticles on gold are measured. Figure 5.1A shows the single particle spectra of 117 particles on a 45nm gold film with a 5nm polymer spacer layer. The resonance wavelength of the longitudinal dipole appears to be ~700nm. However, its resonance wavelength and linewidth vary from particle to particle. This is shown in Figures 5.1B and C, where a normal distribution is used to find the mean and the standard deviation. In order to summarize the variations in the scattering spectra from particle to particle, the results are shown by taking the mean of the single particle spectra, Figure 5.1B, where the shaded part depicts the standard deviation from the mean.
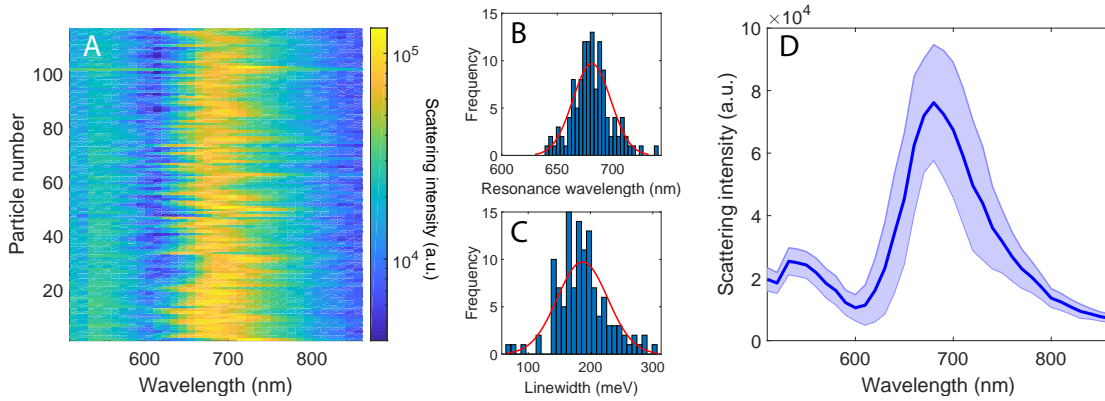

Figure 5.1: Waterfall plot of single-particle scattering spectra for 117 particles on a 45 nm thick film with a 5 nm polymeric spacer. Distributions of the resonance wavelength (B) and the linewidth (C) of the longitudinal dipole mode with a normal distribution fit (red curve).(D) Mean (blue line) and standard deviation (shaded area) of 117 particle spectra.

5.1 Particle geometry

5.1.1 Polydisperse particles

Sigma-Aldrich particles with a diameter of 100nm are spin-coated directly on a 45nm gold film. The TEM image, Figure 5.2A. The particle diameters measured on the major and minor axes show two populations, one with diameters of below 50 nm and one with diameters above 50 nm, 5.2B. The particles with diameters below 50 nm will probably not be observed in the measurements due to their low scattering intensity. The mean diameter of the minor and major axes of the population of larger particles is 93.8 ± 15.0 nm with a mean aspect ratio of 1.15 ± 0.18 nm, Figure 5.2C.
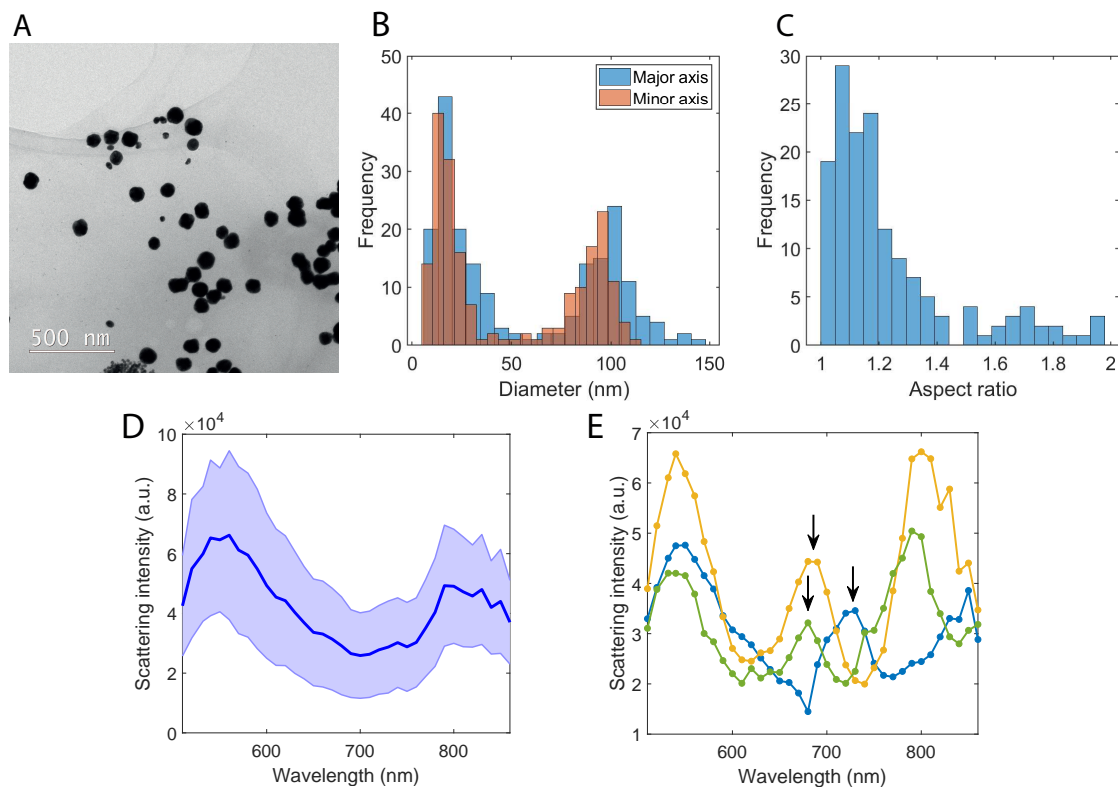
Figure 5.2: (A) TEM image of Sigma-Aldrich 100nm nanoparticles. (B) Dispersion of the diameters of 198 particles measured along the major axis (blue) and the minor axis (red). (C) Histogram of the aspect ratios of 89 particles with a diameter of the major axis larger than 50 nm. (D) Mean (blue line) and standard deviation (shaded area) of 119 Sigma-Aldrich particle spectra.(E) Three measured spectra of individual Sigma-Aldrich particles (blue, green, yellow) with arrows indicating the peaks emerging due to the asymmetry of the particles.

The spectra are measured using dark-field microscopy. According to figure 4.3, three modes should be distinguished: the quadrupole at 540 nm, the transversal dipole at 600 nm and the longitudinal dipole at 750 nm. However, the measured spectra deviate from the simulations, Figure 5.2D. Since the particles are deposited directly on gold, the gaps between the particle and the film are smaller than 1 nm. As

explained in Chapter 4, the BEM calculations fail to predict the plasmonic behaviour at such small gap sizes and can therefore not be compared to experiments.

In roughly $\sim 20\%$ of the individual Sigma-Aldrich particles, a peak is observed that is not predicted in earlier simulations, Figure 4.3. In Figure 5.2E three examples of these spectra are shown, where the arrows indicate the peak of which the origin is not known. Kleemann et al. reported that this peak emerges due to facets on asymmetric particles facing the film [32].

Figure 5.3A shows the bottom view of such a particle. The particle is depicted as an ellipsoid with semi-axes a_x, a_y and a_z with a facet width w_x. Either p- or s-polarized light is incident on the particle from the top with an incidence angle θ and an azimuthal direction ϕ.
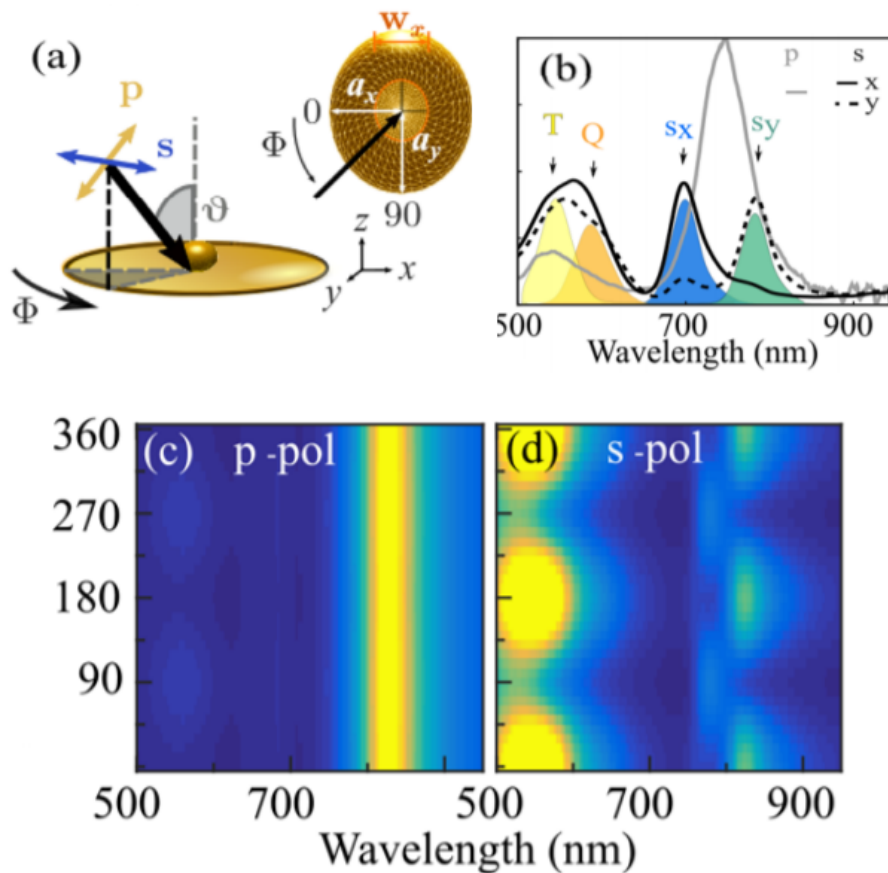
Figure 5.3: (A) Simulation setup, ellipsoid semi-axes a_x and a_y and facet width w_x. (B) Scattering spectra of p-polarized (gray) and s-polarized (bblack) incident light. Orthogonal polarization axes (x, y) within the azimuthal plane (solid, dashed) show different modes. T: transversal dipole, Q: quadrupole, $s_{x,y}$: dark cavity modes. (C,D) Simulated scattering spectra from a nanoparticle on film for p- and s-polarized light. Source: Kleemann et al., *ACS nano*, 2016 [32].

The spectra of a 80nm faceted particle on a gold film for different polarizations and directions are shown in Figure 5.3B. Under p-polarized light illumination the peak at

750 nm can be identified as the longitudinal dipole. Under s-polarized illumination however, the longitudinal dipole disappears as is expected, but two other modes appear in stead, which is not predicted by previous simulations. The intensity of these modes, labeled as s_x and s_y, depends on the illumination direction, as s_x is strongest under illumination from the x-direction and s_y under illumination from the y-direction.

This behaviour is shown in more detail in Figures 5.3C and D, where the scattering spectrum is plotted as a function of azimuthal angle. In the simulations the following geometry parameters are used: a_x=30nm, $a_y = a_z$ =40nm and w_y=25nm. For p-polarized light (Figure 5.3C) there is no dependence on the polarization angle, due to the z-oriented dipole that exhibits a centrosymmetric charge distribution which is independent on the facet asymmetry. For s-polarized light however, the s_x and s_y modes show a clear dependence on the polarization direction, with a 90° phase-shift in their response. Changing the incident azimuthal angle of s-polarized light accesses modes along different facet directions. Both the facet asymmetry and the facet width influence the position of the resonance wavelength of the s_x and s_y modes.

Simulating the surface charge distributions of the modes with the same geometry (a_x=30nm, $a_y = a_z$ =40nm) gives the results in Figure 5.4A. The longitudinal dipole (P) and the quadrupole mode (Q) have surface charge distributions over the entire particle, while the surface charges of the s_x and s_y modes are confined to the gap. Their charge separations are along two perpendicular axes. Since $a_y > a_x$, the surface charge distribution is confined over a smaller surface at s_x than at s_y and will thus have a shorter resonance wavelength. In order to elucidate the origin of these modes, the simulations are compared to an analytical cavity model, Figure 5.4B. In the analytical cavity model of a faceted nanoparticle on a flat film, modes are described as drum-like standing waves, and calculated analytically by

$$\lambda_i(w, d) = \lambda_p \sqrt{w\varepsilon_d/(d\alpha_i) + \varepsilon_\infty}, \tag{5.1}$$

where λ_p is the plasmon wavelength of gold, ε_∞ is the gold background permittivity, ε_d is the gap permittivity, w is the facet width, d the gap size and α_i is the i-th antinode of the $J_0(\alpha)$ cylindrical Bessel function. Even-order modes i are bright modes and odd-order modes are dark. The calculated even modes and odd modes are shown in Figure 5.4B as dashed and solid lines respectively. The s_x- and s_y-mode match equation (5.1) well for mode order i=1, meaning that the s-modes are dark-modes. Usually these modes thus do not radiate into the far-field. However, due to the facet on the nanoparticle, these modes become bright under s-polarized illumination.
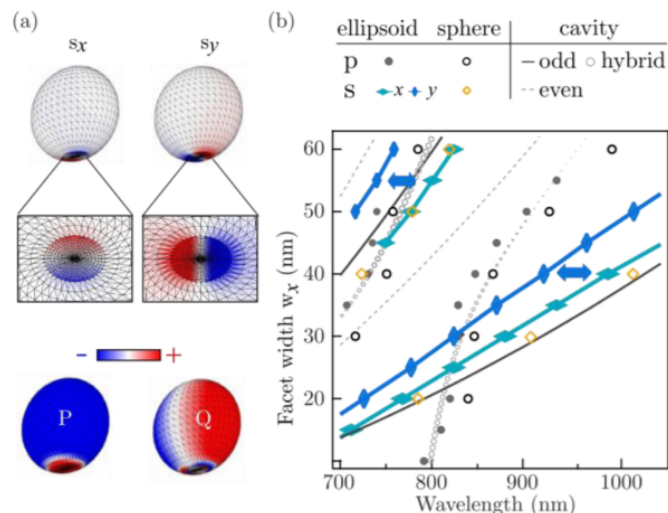
Figure 5.4: (A)Surface charge distributions of a slightly elliptical nanoparticle with a_x=30nm, $a_y = a_z$ =40nm. (B) Comparison of analytical cavity model (gray lines, dark solid = odd, dashed = even) and BEM simulations (blue, orange and gray points). Source: Kleemann et al., *ACS nano*, 2016 [32].

In Figure 5.5 several polarization dependent scattering spectra of faceted nanoparticles are shown. Large variations in the optical response from particle to particle are observed, which is in agreement with the large variety in particle geometries (SEM images).
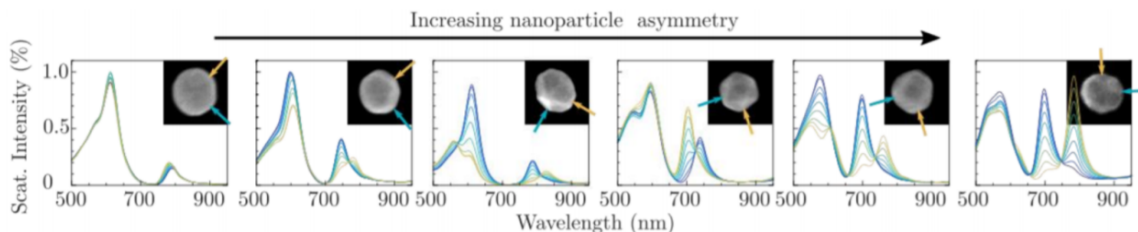
Figure 5.5: Measured scattering spectra for 80nm nanoparticles on film with their SEM images (insets). The orange and blue arrows indicate the polarization angle of maximum intensity for the s_x and s_y modes respectively. Source: Kleemann et al., *ACS nano*, 2016 [32].

In the case of a faceted sphere the s_x and s_y modes can thus be excited using s-polarized light. Due to the strong dependence of these modes on the facet geometry, size and incident azimuthal direction, a large heterogeneity in the single particle spectra is observed.

5.1.2   Ultra-uniform particles

The heterogeneity can thus be reduced by using uniform, non-faceted particles. In Figure 5.6A a TEM image of such particles is shown where the particles show indeed

a large monodispersity in shape.
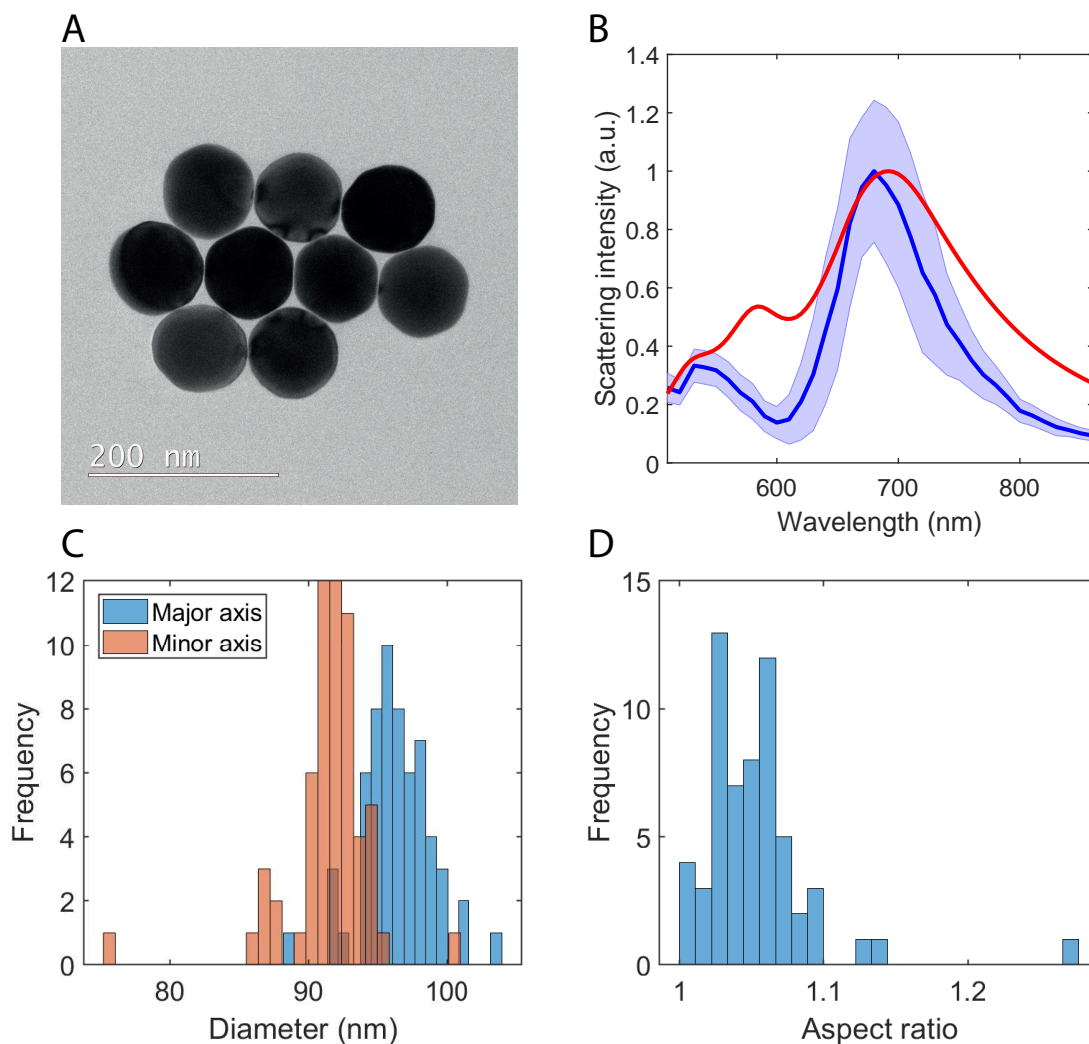
Figure 5.6: (A) TEM image of nanoComposix 100nm nanoparticles. (B) Mean (blue line) and standard deviation (shaded area) of 117 particle spectra. (C) Dispersion of the diameters of 60 particles measured along the major axis (blue) and the minor axis (red). (D) Histogram of the aspect ratios of 60 particles.

These particles are deposited on a 45nm gold film with a 5nm spacer layer. The resulting mean scattering spectrum is shown in Figure 5.6B where the measured mean spectrum is compared to a simulation. The spacer thickness is estimated by comparing the longitudinal dipole resonance wavelength of the measurements with simulations, which gives the best match for a 5nm spacing, Figure 5.6B. This is well above the spacing of 1nm, so non-classical effects do not need to be taken into account and BEM calculations can accurately predict the optical response. When comparing the mean spectrum of the nanoComposix particles, Figure 5.6B, to that of the Sigma-Aldrich particles, Figure 5.2B, a decrease in the average relative standard deviation is found from 47% for the Sigma-Aldrich particles to 31% when using nanoComposix particles. This is caused by the reduced heterogeneity with respect to the Sigma-Aldrich particles, as the mean particle diameter of the major and minor axes exhibits

34

a smaller standard deviation 94.0 ± 3.7 nm, Figure 5.6C, and the mean of the aspect ratio of the nanoComposix particles is much closer to 1: 1.05 ± 0.04 nm, Figure 5.6D.

Due to the increased heterogeneity in optical response, in further experiments nanoComposix particles are used.

5.2   Sample-to-sample heterogeneity

The heterogeneity from particle-to-particle is thus reduced by using ultra-uniform nanoComposix nanoparticles. Three samples are prepared where nanoComposix particles are deposited on 45 nm films with 5 nm spacings. The measured spectra are shown in Figure 5.7A where all three samples show a plasmon resonance at approximately the same wavelength, from top to bottom: 681 ± 17 nm, 683 ± 19 nm and 678 ± 22 nm. The heterogeneity from sample-to-sample is thus found to be low when using nanoComposix particles, meaning that a high reproducibility is obtained.
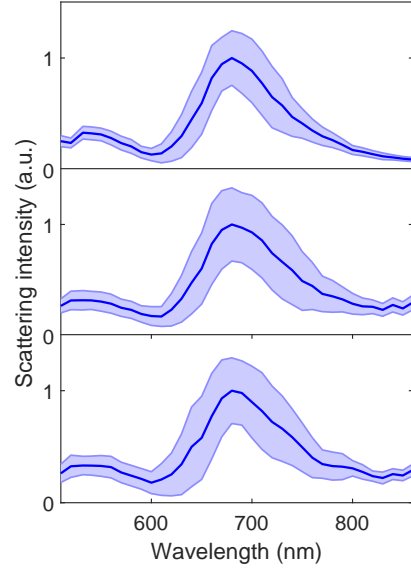
Figure 5.7: Mean and standard deviation of the spectra, measured on three samples with 117 (top), 139 (middle) and 188 (bottom) nanoComposix particles on a polymer spacer on a 45nm gold film.

5.3   Residual heterogeneity

Several parameters could contribute to the residual heterogeneity found in Figure 5.7, such as the slight asphericity of the particles, Figure 5.6C and small deviations in the particle-film spacing. Furthermore, Lumdee et al. reported that roughness in the film can lead to a shift in the longitudinal dipole resonance. The sensitivity to the surface roughness is caused by the tight confinement of the field, which makes the plasmon resonance sensitive to the geometry near the gap at small spacings. Lumdee et al. showed that when simulating the coupling between a particle and a film with a roughness of $R_q = 1.2$ nm, a red-shift in the longitudinal dipole wavelength of 5 nm is found [70]. The measured surface roughness of 45nm gold films used for the experiments is found to be even lower, $R_q = 0.3 - 0.6$ nm, so shifts < 5 nm can be expected due to the roughness on the films.

Also, the refractive index around the nanoparticles influences the longitudinal dipole resonance wavelength, Figure 4.7, especially in the highly sensitive gap region. It is not unlikely that the refractive index in this region varies from particle to particle, which would contribute to the heterogeneity in the optical response. The particles are functionalized with either citric acid (Sigma-Aldrich), or PEG-Carboxyl (nanoComposix). The density of the coverage could vary from particle to particle. Also, water

could be left over in the gap after drying the sample. Variations in the volume of the water in the gap leads to varying longitudinal dipole resonance wavelengths. Figure 5.8A shows simulated spectra of a particle on a 45nm film with a 1nm spacing and varying refractive indices in the gap. A refractive index in the gap region is added by simulating a 1nm layer with a certain refractive index between the particle and the gold film. The simulations show that varying the refractive index leads to a shift in the longitudinal dipole resonance wavelength. Variations in the refractive index in the gap region thus contributes to the heterogeneity from particle-to-particle.
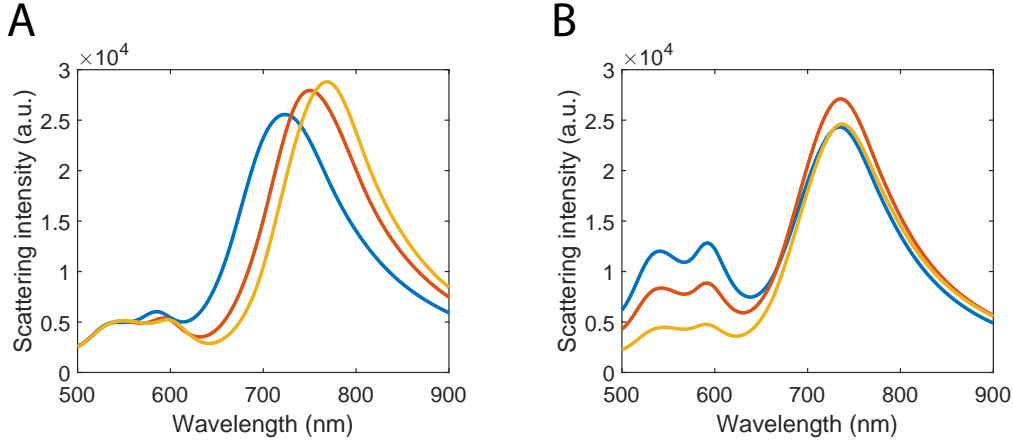
Figure 5.8: (A) Simulated spectra of a nanoparticle on a 45nm film with a 1nm spacer layer with a refractive index of $n = 1$ (blue), $n = 1.3$ (red) or $n = 1.5$ (yellow). (B) Simulated spectra of a nanoparticle on a 45nm film with a 1nm spacing with incident light under an angle of 53° (blue), 62° (red) or 72° (yellow).

The NA of the dark-field condenser lies between 0.8 and 0.9, which means that the incident light excites the particles under angles of between 53° and 72°. Figure 5.8B shows that varying the incident angle does not change the resonance wavelength of the longitudinal mode, but it does change the scattering intensity of the quadrupole and transversal dipole modes, which can be attributed to varying contributions of s-polarized and p-polarized light to the optical response with varying incident angle, as is explained in Section 4.4. Since the incident light on the sample is a mix of light coming from all angles between 53° and 72°, different particles might be excited under different angles, which adds another contribution to the heterogeneity.

Chapter 6

Film thickness and particle-film spacing

As explained in the previous chapter, ultra-uniform nanoComposix particles exhibit a higher homogeneity in the particle scattering spectra with respect to the Sigma-Aldrich particles. Therefore, nanoComposix particles will be used in further experiments in order to achieve a high reproducibility. The influence of the film thickness on the far-field and near-field optical response is assessed, in order to propose an optimal film thickness for sensing where the intensity of the longitudinal dipole is high and the intensity at a probe wavelength shifts significantly as the particle-film spacing is varied. First, the response of the particle scattering spectrum on varying the gold film thickness is assessed. Next, the influence of the particle-film spacing on the scattering spectrum is investigated. Finally, an optimal film thickness is proposed for sensing, based on the intensity of the scattering spectra and intensity changes upon varying the spacing on different film thicknesses.

6.1   Film thickness

Again hyperspectral microscopy was used to measure the spectra of particles on a gold film. However, the thickness of the gold film is varied. Samples are prepared with a 10 nm, 15 nm, 30 nm and 45 nm gold film. Four single polymer layers, corresponding to a 5 nm spacer, are deposited on each sample as explained in Chapter 3, after which the nanoComposix particles are spin-coated.

The resulting spectra are shown in Figure 6.1 together with the simulated spectra of this system. Two peaks can be identified: the quadrupole at $\sim$540 nm and the longitudinal dipole at $\sim$690 nm. The resonance wavelengths of these modes do not change as the film thickness is varied. The ratio in intensity between the longitudinal dipole and quadrupole mode changes for varying film thicknesses from approximately 3:1 for the 45 nm film to 1:1 for the 10 nm film, which is similar to what is observed in the simulated spectra. However, in earlier simulations a decrease in the longitudinal dipole scattering intensity is observed, Figure 4.6, which is explained by the reduced
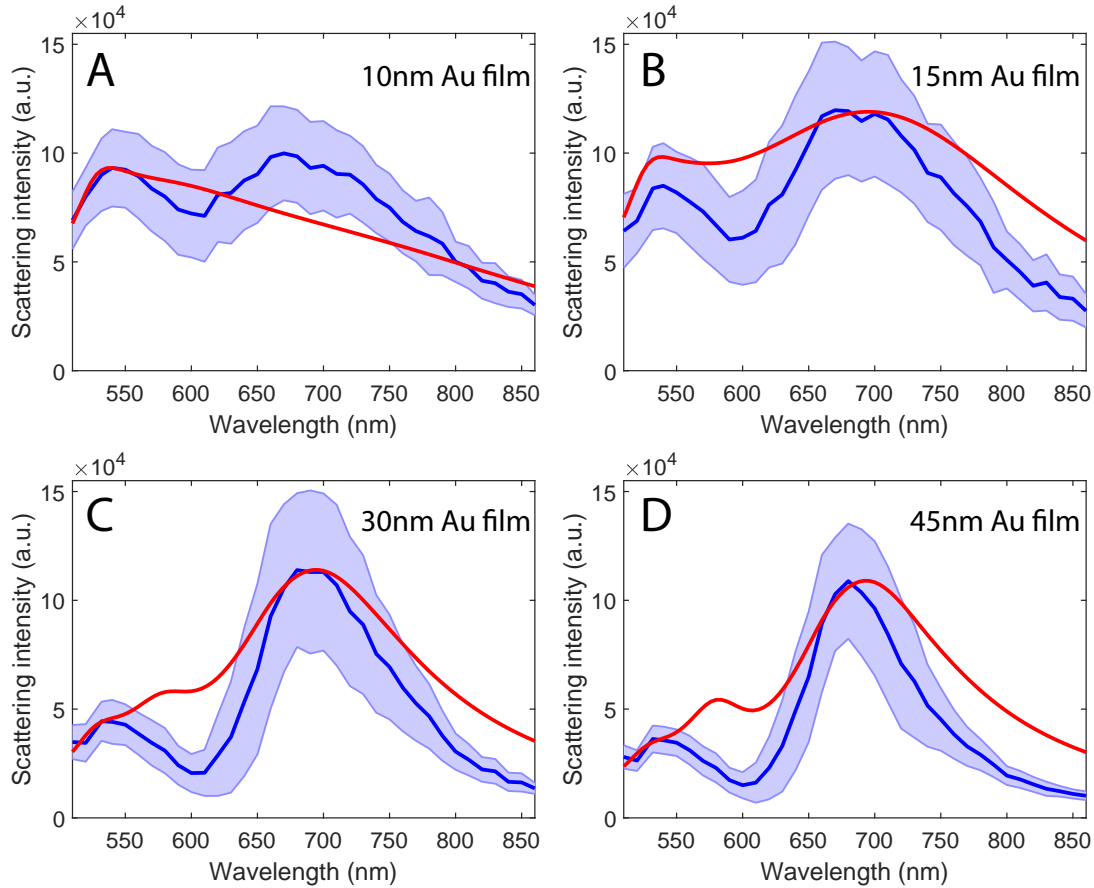
Figure 6.1: (A-D) Mean and standard deviation of the spectra of 100 nm nanoComposix nanoparticles, measured on varying gold film thicknesses:(A) 115 nanoparticles on a 10 nm film; in (B) 116 nanoparticles on a 15 nm film; in (C) 136 particles on a 30 nm film; and in (D) 117 particles on a 45 nm film. Red lines show the simulated far-field spectra.

dipole moment between the nanoparticle and the image charges in the film as the thickness decreases. This is not observed in the measurements, where the intensity of the longitudinal dipole remains roughly constant. These higher collected intensities are caused by the increased transmission of light through thinner film, Appendix C, which is not taken into account in the simulations. Due to the higher transmission, the intensity decrease in the longitudinal dipole is not observed in experiments.

A second effect that is observed is that with decreasing film thickness the linewidth of the longitudinal dipole increases. Sobhani et al. studied this effect for aluminium nanoparticles on a varying aluminium film thickness [71]. It is hypothesized that the longitudinal dipole exhibits a narrower linewidth when coupled to a film due to a decrease in the radiation damping. Decreasing the film thickness leads to a less tight confinement of the field in the gap and thereby an increased relation damping, which thus results in a broader linewidth. Further research needs to be conducted in order to confirm that an increased radiation damping really is the mechanism that leads to a linewidth broadening on decreasing film thicknesses and is discussed in 7

Interestingly, the transversal dipole is not visible in the measurement, even though this mode is observed in the simulations. The calculations on the scattering cross-section include contributions in all directions. In reality, light is collected via the objective, meaning that light scattered in other directions is not collected. The radiations pattern differs per mode and is not homogeneous in all directions, Figure 6.2. The collected intensity thus depends on the mode and on the position of the objective with respect to the particle and its collection angles. Possibly, when measuring from below ($z < 0$), as is the case in the experiments, the objective will collect only a small fraction of light scattered by the transversal dipole, whereas the radiation patterns of the quadrupole and longitudinal dipole are more directed towards the objective.
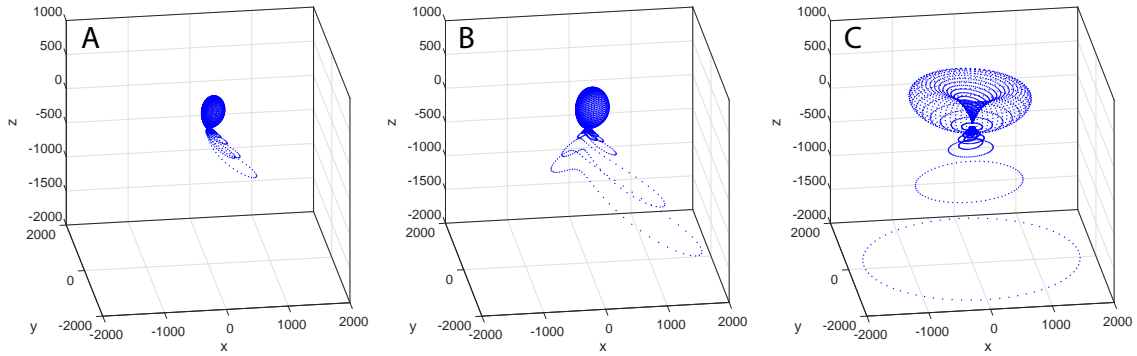

Figure 6.2: Radiation patterns of 100 nm gold particles on a 45 nm gold film with a 5 nm spacer of the (A) quadrupole, (B) transversal dipole and (C) longitudinal dipole. The top of the spacer layer is situated at z=0.

The calculated dependency of the far-field spectra on the film thickness is shown in more detail in Figure 6.3A. For films thicker than ∼40 nm the scattering intensity at the longitudinal dipole mode remains constant, while for thinner films the intensity decreases gradually. Not only the longitudinal dipole, but also the transversal dipole decreases in intensity for a decreasing film thickness. This could also be due to the incomplete image dipole at thinner films, which decreases the dipole moment, such that less light is radiated from the transversal dipole as well.

The measured resonance wavelengths and linewidths of the longitudinal dipole are compared to simulations in Figure 6.3B. Apparently, the measured linewidths are consistently smaller than what is predicted by simulations. In Chapter 2 the different influences on linewidth broadening are explained. One, or more, of these damping effects is thus smaller than predicted. Small variations in the nanoparticle diameter are observed in the TEM image, Figure 5.6A, which influences the contributions of surface scattering and radiation damping. Surface scattering is reduced by increasing the nanoparticle diameter. However, for particles larger than 40 nm surface scattering is not a significant influence and further increasing the particle diameter will thus not narrow the linewidth. On the the other hand, larger particles exhibit a larger radiation damping and will thus exhibit a linewidth broadening. Radiation damping could explain the linewidth narrowing if a large portion of particles is smaller than 100 nm in diameter. In Figure 5.6C the distribution of nanoComposix particle diameters
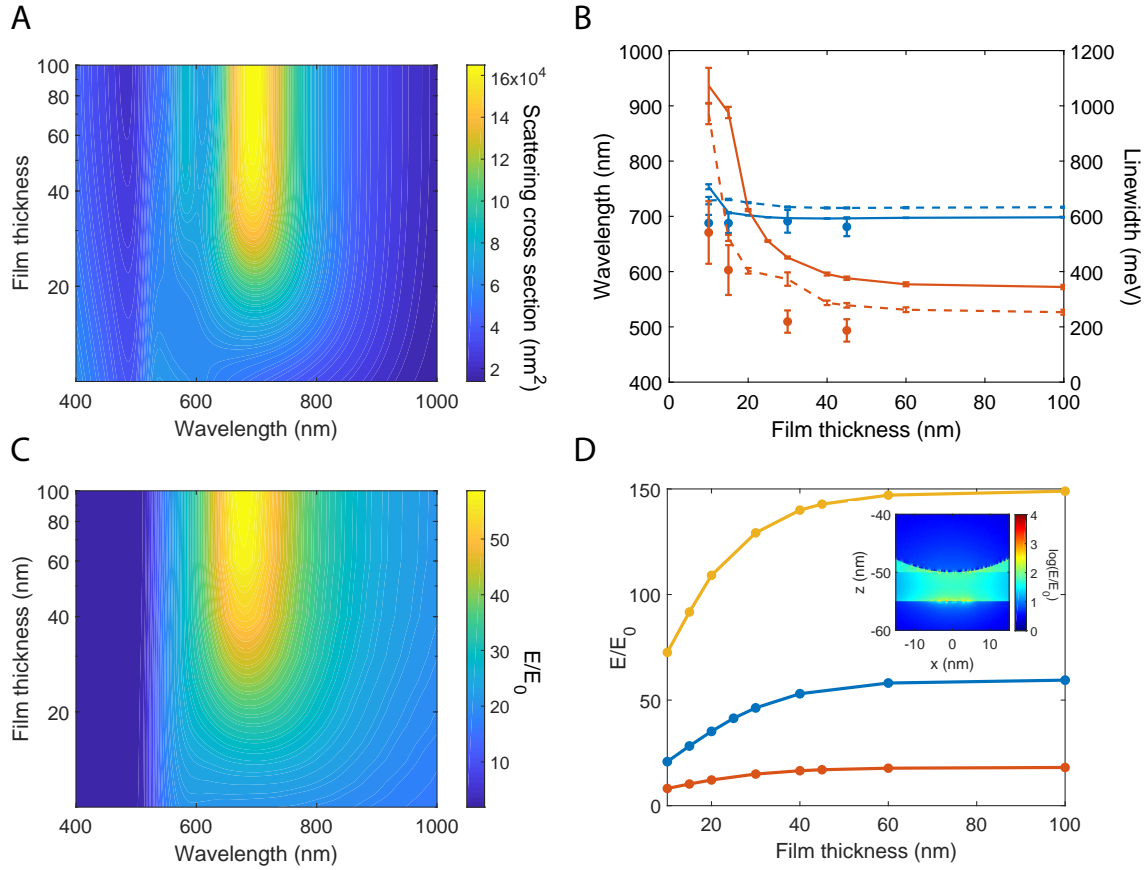
Figure 6.3: (A) Calculated far-field spectra of a gold nanoparticle with a 5 nm spacer above gold films of varying thicknesses. (B) Effect of film thickness on the longitudinal dipole mode resonance wavelength (blue) and linewidth (red). The blue (red) line represents the calculated longitudinal dipole mode resonance wavelength (linewidth), while dots represent the measured values. Error bars on the experimental data are the standard deviation of the normal distribution for the single-particle spectra measured for each sample. (C) Calculated near-field spectra of a gold nanoparticle with a 5 nm spacer above gold films of varying thicknesses. The near-field is calculated at the center of the gap region at 2.5 nm above the gold film. (D) Relationship between the near-field enhancement and gold film thickness, for a 1 nm (yellow), 5 nm (blue) and 10 nm (red) spacing. The near-field enhancement at the center in the nanoparticle-film gap is plotted. The inset shows an example near-field calculation in the nanoparticle-film gap (gold film thickness 45 nm, 5 nm spacing).

is shown, where a mean diameter of 94 ± 3.7 nm is found. Even though this is smaller than 100 nm, when decreasing the particle diameter from 100 nm to 90 nm, a linewidth narrowing of only ∼30 nm is observed. Therefore, the slightly smaller diameter of the nanoComposix particles compared to the simulated particles does not explain the difference in measured and simulated linewidths. Another effect that could narrow the linewidth is a reduced electron-defect scattering. However, in calculations an ideal particle is simulated, which will therefore have no defects. This can thus not explain the narrower linewidth of the measured plasmon resonances with respect to the simulations. What is left is the bulk damping. Possibly an unsuitabel

dielectric function of gold is used in the simulations. In simulations the dielectric function as measured by Johnson & Christy [45] is used. However, literature values vary on the appropriate optical constants of gold 2.1. Even the deposition method can be of influence [72]. Therefore, the measured longitudinal resonance wavelengths and linewidths are also compared to simulations using the dielectric function according to Palik [46] in Figure 6.3B, dashed line. The simulated linewidth using Palik's dielectric function are still broader than the measured linewidths, but are narrowed with respect to the previous simulations and thus closer to the measured values. The resonance wavelength however is red-shifted with respect to the measured wavelength, meaning that according Palik's dielectric function, the spacing is slightly larger than 5nm. Not only the dielectric function of gold, but also of the 5 nm chromium adhesion layer can influence the linewidth. For the chromium layer the dielectric function as measured by Johnson & Christy is used. However, for thin films the dielectric function of chrome varies a lot from that of the bulk [73], which will thus have an effect on the scattering spectra, especially when the gold film thickness is thinner than the skin depth of gold, ∼44 nm.

The stronger coupling between the particle and film at thicker films, can also be observed in the near-field enhancement in the gap. The near-field enhancement is calculated in the middle of the gap, 2.5 nm above the gold film. In Figure 6.3C the resulting near-field spectra as a function of film thickness are shown. Also in the near-field enhancement the longitudinal dipole increases for increasing film thickness until it saturates. The near-field spectra are broadened with respect to the far-field spectra due to constructive interference between the near-field and incident field on the red wing of the longitudinal dipole mode. The field enhancement is largest at the longitudinal dipole mode, which is shown for a 45 nm gold film in Figure 4.3 in Chapter 2. The field enhancement at the gap center is thus plotted at the longitudinal dipole resonance in Figure 6.3D, where it is observed that the near-field enhancement gradually increases from $\frac{E}{E_0} = 20$ at a 10 nm film thickness until it saturates at $\frac{E}{E_0} = 60$ for films thicker than 45 nm. These results are compared to simulations on 1 nm and 10 nm spacers. For an increasing spacing the near-field enhancement between the particle and the film decreases. However, also on the 1 nm and 10 nm spacer the near-field enhancement saturates at a film thickness of 45 nm. Not only the film thickness, but also the particle-film spacing thus influences the near-field enhancement in the gap region.

6.2   Particle-film spacing

The particle-film spacing thus has an effect on the near-field enhancement in the gap region. In order to gain more insight into the effect of the particle-film spacing on the optical response the scattering spectra of nanoparticles on a film are measured as well as simulated for varying spacer thicknesses.

Polymer spacer layers are deposited onto 30 nm gold films as explained in Chapter 3. Four samples are prepared with either 0, 2, 4 or 6 polymer layers, corresponding to 0 nm, 2.5±0.5 nm, 5.3±1.2 nm and 17.7±3.8 nm spacings respectively, Figure

3.2. NanoComposix particles are deposited on top of these layers and the spectra are measured via dark-field microscopy. The resulting spectra are shown in Figure 6.4, together with simulated spectra. The longitudinal dipole resonance clearly blue-shifts as the spacing between the particle and film is increased, with a total shift of ∼200 nm between no spacer and 6 polymer spacer layers (17.7±3.8 nm). In Chapter 4 it is already discussed that no accurate predictions on the optical response of the particle on a film with no spacer layer (Figure 6.4A), since the model does not include the effects of quantum tunnelling and electron delocalization.
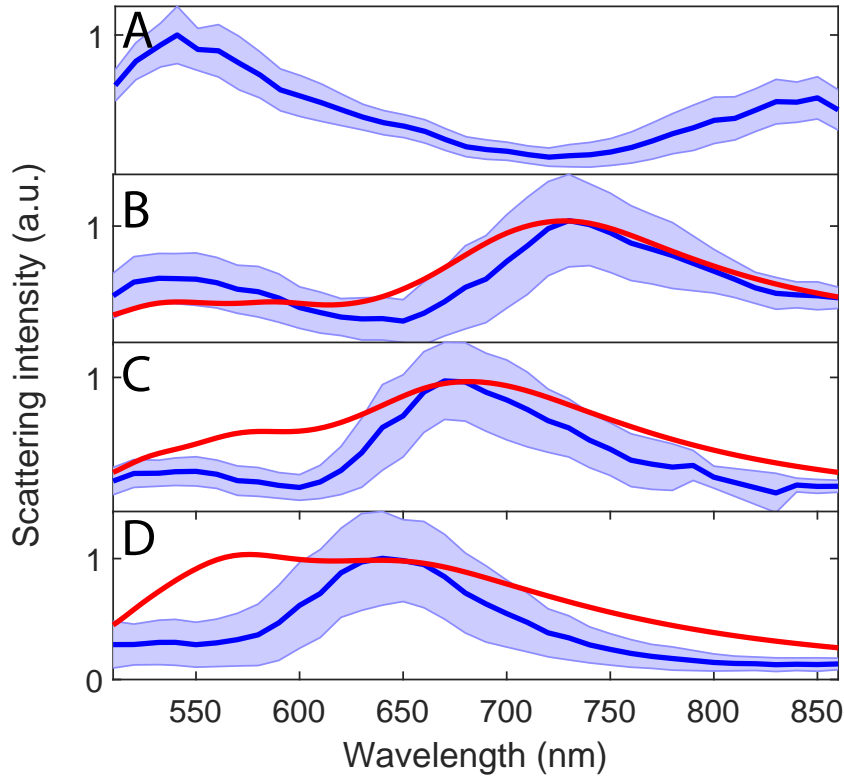
Figure 6.4: (A-D) Mean and standard deviation of the spectra of nanoparticles, measured on varying numbers of polymer layers:(A) 127 nanoparticles on 0 layers; in (B) 134 nanoparticles on 2 layers; in (C) 116 particles on 4 layers; and in (D) 139 particles on 6 layers. Red lines show the simulated far-field spectra for spacings of (A) 1 nm, (B) 3 nm, (c) 6 nm and (D) 10 nm.

The 2 layers spacer and 4 layers spacer are compared to simulations with a 3 nm and 6 nm spacer respectively, which corresponds well to the measured spacer thicknesses of 2.5±0.5 nm and 5.3±1.2 nm. However, the spectra with a spacer of 6 layers correspond to the simulation of a 10 nm spacer, which is thinner than the measured thickness of 17.7±3.8 nm. Inhomogeneities the thickness of the spacer layer of a few nanometers have been reported on these polymers previously [74]. Possibly, the measurements were taken on a thinner part of the spacer. Also, the particles could gradually sink into the spacer layer, such that the spacing decreases. A better control over the spacer layer thickness is needed in order to know the exact nanoparticle-film spacing.

The shift in the resonance of the longitudinal dipole can be explained by considering the interaction of a nanoparticle with its image in the film. When light is incident on a particle, the charges get displaced. Negative and positive charges thus reside on opposite sides of the sphere. This results in a restoring force leading to a resonance condition, as explained in Chapter 2. When the particle is in the vicinity of a gold film, the longitudinal- and transversal dipole mode are red-shifted due to opposite charges in the particle and film facing each other in the gap region, as depicted in Figure 6.5. The net charge is thus spaced further apart which reduces the restoring force in the particle and thus results in a lower resonance frequency. Increasing the distance between the particle and the film diminishes the attractive force between charges in the particle and the film, which results in an increasing resonance frequency. Also, as the resonance frequency increases the amplitude of the oscillation, and thereby the intensity of the radiated field, decreases. The quadrupole will not show significant shift since only a small fraction of the charges are confined near the surface.
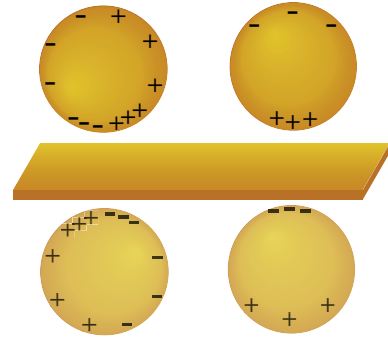

Figure 6.5: A horizontally polarized (left) and a vertically polarized (right) particle with their surface charge distributions and their images in the film (bottom).

Although the spectra of the particles on 2 and 4 polymer layers, Figures 6.4B and C, show a good correlation with the simulations, on 6 polymer layers the ratio between the intensity of the quadrupole and longitudinal dipole peaks does not correspond to the simulation. While the simulation shows a ratio of 1:1, the measured intensity of the longitudinal dipole is approximately five times larger than that of the quadrupole. This is probably due to a shift in the transversal dipole resonance so that it overlaps with the quadrupole in the simulation. In Figure 6.6A the spectrum of a nanoparticle on a 10nm spacer layer is simulated for excitation with p-polarized light and s-polarized light, and a superposition of these spectra. S-polarized light excites both the quadrupole and transversal dipole mode as explained in Chapter 2. However, only one peak is observed instead of two in the simulation for s-polarized light in Figure 6.6A. In order to find out why only one peak is observed, the spectra for s-polarized excitation are shown as a function of spacing in Figure 6.6B. For decreasing spacings, the transversal dipole red-shifts and decreases in intensity, while the quadrupole remains constant in resonance wavelength and intensity. The peak at ∼570 nm in Figure 6.4D is thus a superposition of the transversal dipole and quadrupole. The simulated peak ratio at the 10 nm spacing in Figure 6.4D is thus the ratio between the longitudinal dipole peak intensities and a superposition of the intensities of the transversal dipole and quadrupole peaks. However, in Chapter Section 6.1 it is already discussed that the transversal dipole is in many cases not observed in measurements, possibly due to its radiation pattern and the collection angles of the objective as explained in Section 6.1. It would thus be incorrect to compare the peak ratio of the simulated spectrum to that of the measured spectra, since in the measurements the transversal dipole does most likely not contribute to the peak intensity of the peak at ∼540 nm. In Figure 6.6B it is observed that the

calculated scattering cross-section of the quadrupole alone is ~ 2000 nm^2. When comparing this to the calculated scattering cross-section of the longitudinal dipole in Figure6.6A (~ 8000 nm^2), a ratio of 1:4 is found which is much closer to what is observed in experiments, Figure 6.4D.
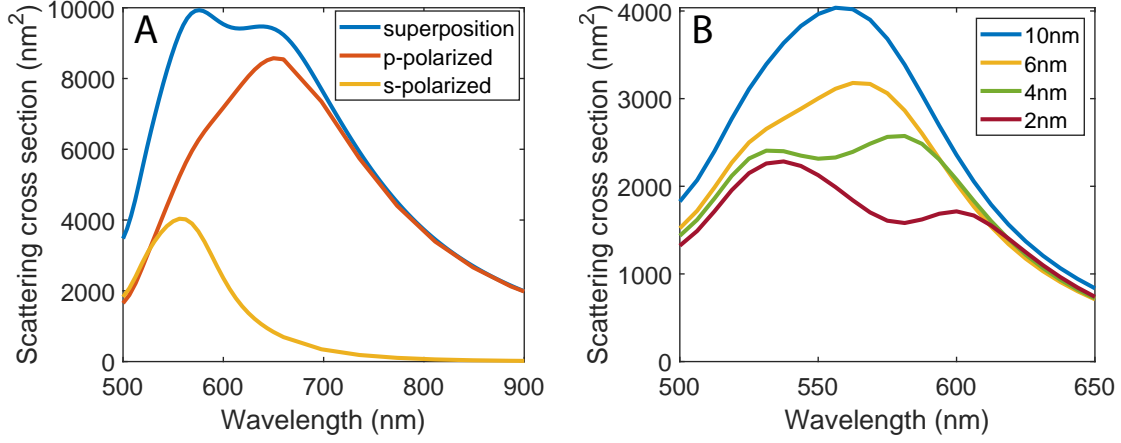

Figure 6.6: (A) Simulated spectra of a particle on a 30nm film with a 10nm spacer layer for p-polarized, s-polarized excitation and a superposition of these spectra. (B) Simulated spectra for varying spacer layer thicknesses with s-polarized light.

The calculated dependency of the far-field spectra on the particle-film spacing is shown in more detail in Figure 6.7A. The longitudinal dipole blue-shifts when increasing the spacing as is observed in experiments (Figure 6.4). Over a range of 10 nm, the resonance of the longitudinal dipole shifts ~ 200 nm to the blue, with the largest shifts at small spacings, Figure 6.7B, due to the tight confinement of the electric field at small spacings and therefore the high sensitivity to changes in spacing. Also, the transversal dipole resonance blue-shifts slightly from ~ 630 nm to ~ 580 nm. Also a decrease in the longitudinal dipole resonance is observed due to the decreasing amplitude of the electron oscillations for an increasing resonance frequency.

In the previous section it is already briefly discussed that the particle-film spacing influences the near-field enhancement in the gap. This is shown in more detail in Figure 6.7C, where the near-field enhancement is largest at small spacings. At a spacing of 1 nm, the field is enhanced more than 200 times, while at a 10 nm spacing the field enhancement decreases to $\frac{E}{E_0} = 20$, since opposite charges in the particle and film are closer together when the spacing is small and thus a stronger field will be induced.
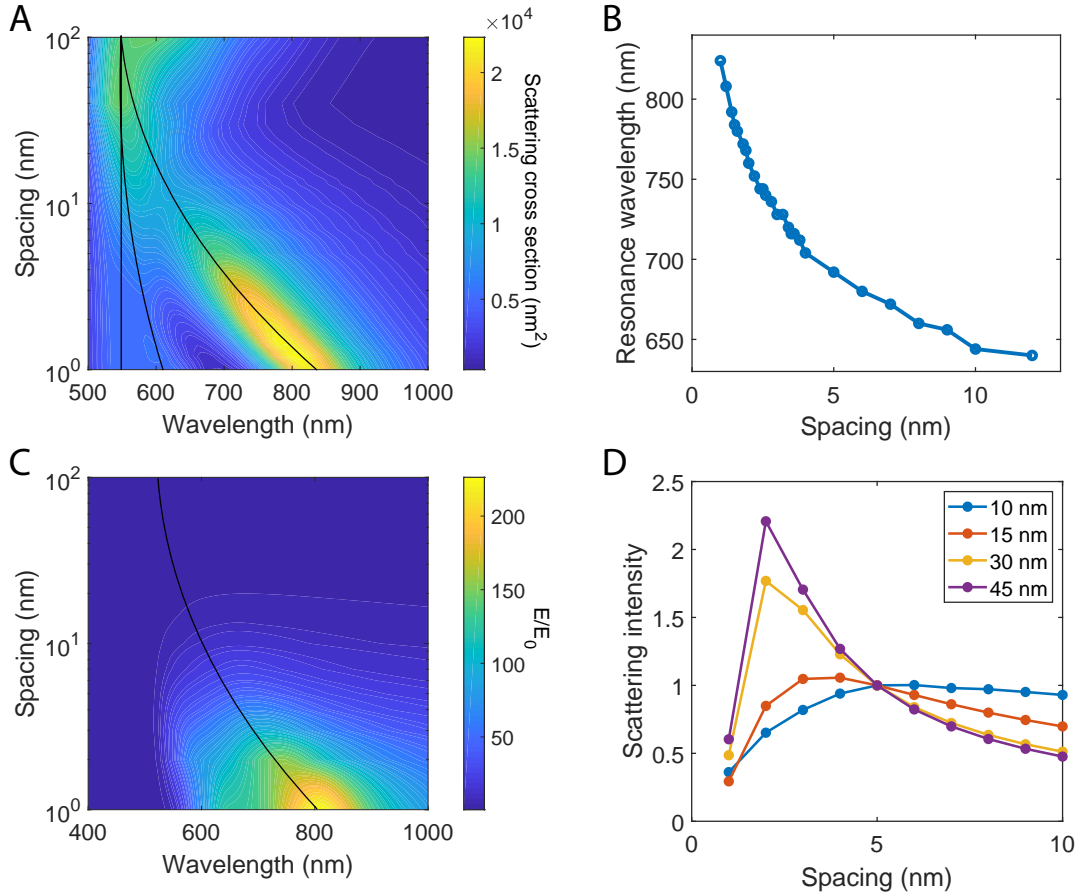
Figure 6.7: (A) Calculated far-field spectra of a 100 nm nanoparticle with a varying spacing above 30 nm gold film. Black lines indicate the positions of the quadrupole, transversal dipole and longitudinal dipole. (B) Calculation of the longitudinal dipole resonance wavelength of a 100 nm nanoparticle on a 30nm gold film as a function of the spacing. (C) Calculated near-field spectra of a 100 nm nanoparticle with a varying spacing above a 30 nm gold film. The near-field is calculated at the center of the gap region. The black line indicates the position of the dipole (D) Calculated scattering cross section of a 100 nm nanoparticle on a 10 nm, 15 nm, 30 nm and 45 nm gold films as a function of spacing.

The resonance wavelength thus blue-shifts for increasing spacing. In the previous section it is discussed that decreasing the film thickness leads to a broader linewidth. When probing the scattering intensity at one wavelength for varying spacer thicknesses, smaller intensity changes are thus expected for films thinner than the skin depth of gold. In order to quantify the intensity change, the normalized scattering intensity at a probe wavelength of 700 nm as a function of the particle-film spacing is plotted for varying film thicknesses in Figure 6.7D. The scattering intensities of the four films are normalized to the scattering intensity at a 5 nm spacing, since Figure 6.4 shows that on all film thicknesses a similar intensity is found at a wavelength of ~ 700 nm. Figure 6.7D shows that films with a thickness of 10 nm and 15 nm exhibit indeed a smaller change in intensity upon variations in the spacing. While decreasing

the spacing from 10 nm to 2 nm on a 45 nm film leads to an intensity increase of 450%, on a 10 nm film the intensity does not change significantly when decreasing the spacing from 10 nm to 5 nm after which it decreases to 30% of its initial value. This due to the narrower linewidth of the spectrum of a particle on a 45 nm film and thus a steeper slope.

Even though simulations predict that the intensity of the longitudinal dipole decreases with decreasing film thickness, measurements show that similar intensities can be detected due to the higher transmission of thinner films. However, the linewidth increases with decreasing film thickness, possibly due to an increased rate electron-surface scattering. Even though similar intensities can be detected on all film thicknesses, intensity changes upon shifts in the longitudinal plasmon resonance at a probe wavelength will be larger for spectra with narrower linewidths. Since the 30 nm and 45 nm films exibit the narrowest linewidths, these seem the most appropriate for the proposed biosensor, where the presence of analytes will be measured via intensity changes upon plasmon shifts.

Eventually, the tethered particle biosensor will measure conformational changes of the tether by probing the intensity of the light scattered by the particle at a probe wavelength. The intensity of the scattered light and the changes in scattered intensity should be high enough to be detectable. Measurements show that the film thickness does not significantly influence the scattering intensity of the longitudinal dipole. Even though the dipole moment between the particle and its image in the film reduces for a decreasing film thickness, the transmission increases for decreasing film thickness. The scattering intensities at the longitudinal dipole resonance are therefore comparable for all film thicknesses and the suitability for sensing thus depends on the change in intensity as the spacing varies. The intensity at a probe wavelength of 700 nm changes most for a film thickness of 45 nm, due to the narrow linewidth of the longitudinal dipole. This will thus be the most suitable film thickness for sensing.

Some observed phenomena remain unexplained. The transversal dipole is not observed in the measured spectra, even though simulations show a transversal dipole peak. It is hypothesized that the radiation pattern of this mode is not directed towards the dipole. Also the measured linewidth is consistently smaller than the simulated linewidth. Using different dielectric functions of gold turns out to have a significant impact on the scattering spectrum. More knowledge is needed on the actual dielectric function in order to accurately simulate the scattering spectrum of a nanoparticle on film system. Approaches in order to gain more insight into these phenomena are discussed in Chapter 7.

A blue-shift in the longitudinal dipole resonance of ∼200 nm is observed when increasing the particle-film spacing from 0 nm to 10 nm, due to the increasing restoring force within particles as the spacing increases. A good correlation was found between simulations and measurements except for the measurements on the spacer consisting of 6 polymer layers. According to simulations the particle-film spacing on the 6 polymer layer spacing is 10 nm, which does not correspond to the measured thickness of 17.7±3.8 nm. This could be due to variations in the spacer layer thickness, or particles slowly sinking into the polymer layer. Also, the measured ratio between the quadrupole and longitudinal dipole peaks differs from simulations, possibly due to

the radiation pattern of the transversal dipole, as explained Section 6.1. A suggestion for a better control over the spacer layer thickness is proposed in Chapter 7.

Chapter 7

Conclusions and outlook

The nanoparticle-tether-film system is proposed as a geometry for a plasmonic biosensor. The particle will be tethered to the surface, where the tether is an aptamer for analytes. Before looking into the dynamics of the system it is interesting to analyse different aspects of the plasmonic response. Hyperspectral microscopy is used in order to measure the spectra of hundreds of particles simultaneously.

In Chapter 5, the effect of particle shape on the heterogeneity in optical response is assessed. Polydisperse, faceted particles (Sigma-Aldrich) are compared to to smooth, monodisperse particles (nanoComposix). The relative standard deviation in the measured spectra decreases from 47% for Sigma-Aldrich particles to decreases 31% for nanoComposix particles. Due to the smoothness and high symmetry of the nanoComposix particles, the scattering spectra measurements show a high reproducibility. Residual heterogeneity can be caused by small deviations in particle shapes and sizes, roughness in the particle film, local variations in the refractive index and varying angles of incidence.

In Chapter 6, the influence of the gold film thickness and the particle-film spacing on the near- and far-field response are assessed. According to simulations the longitudinal dipole decreases in intensity as the film thickness decreases while its resonance wavelength stays constant. However, in the measurements no decrease in the longitudinal dipole intensity is observed, due to the higher transmission of light in thinner films. Also, The measured linewidths of the longitudinal dipoles are consistently smaller than the simulated linewidths. Further research needs to be conducted to elucidate the cause. Simulations on the near-field show that the near-field enhancement decreases for thinner films. This is due to the decreased dipole moment between a particle and the film when the film thickness is smaller than the skin depth of gold. The tunability of the field enhancement while keeping the resonance wavelength constant can be used in order to study the effect of field-enhancements on fluorescence and SERS. The field enhancement can be tuned without changing the gap size, material or particle immobilization chemistry, which affect the resonance wavelength of the nanoparticle on film and thus changes the spectral overlap between the emitter and resonance. This enables studies on the transition from the weak coupling to the strong coupling regime [75] and plasmon-enhanced electrochemistry

[76] with various degrees of field enhancement. Also the dependency of the optical response of nanoparticles to the spacing from the film is investigated. NanoComposix particles are deposited on either 0, 2, 4 or 6 spacer layers on 30nm films. The resulting spectra correspond well to simulations. However, according to the spectra of the nanoparticles the 6 layers spacer is thinner than what is measured using ellipsometry. Possibly, there are large variations in the spacer thickness. Overall a 200nm blue-shift is observed when increasing the spacing from 0 to 6 layers, which corresponds to a increase from a 1nm to a 10nm spacing. In order to propose a suitable film thickness for biosensing, the change in intensity at a probe wavelength as the spacing varies is assessed for varying film thicknesses. Due the narrow linewidth of the longitudinal dipole the 45 nm film shows the largest intensity changes for varying spacings, which makes this the most suitable film thickness for sensing.

For future research it will be interesting to gain more insight in the following:

- Even though the spacer layer thicknesses are measured for varying numbers of layers, little is known about what is the actual particle film distance, due to variations in the spacer thickness and the possibility of particles sinking into the spacer. In order to overcome this problem the spacer layer could be deposited using atomic layer deposition of a dielectric, such as Al_2O_3, where the root-mean-square roughness is found to be low: $R_q = 0.43$nm [77], meaning that there are no large deviations in spacer thickness. This allows for more accurate simulations, since the spacer layer is known and varies very little from particle to particle.

- The transversal dipole is not observed in experiments, even though it is present in simulations. The simulations consider the scattered light in all directions, but in reality scattering spectra are measured using only the light that is collected by the objective. Simulated radiation patterns in Figure 6.2 show that the radiation pattern differs per mode. It is hypothesized that the transversal dipole does not radiate in the direction of the objective. Simulating the far-field scattering spectrum taking into account the wavelength-dependent radiation pattern and the collection angles of the objective could confirm if this is the reason that the transversal dipole is not observed in the measurements. Experimentally, the sample could be illuminated from the bottom so that the radiation in another direction is collected. Measuring the scattering spectra when illuminating the bottom of the sample will thus give more insight into the radiation patterns of the different modes.

- The linewidth of the longitudinal dipole broadens as the film thickness decreases. It is suggested that this is caused by an increase in the radiation damping. In order to confirm this, measurements could be done on the spectra of particles on film for a varying electric field confinement in the gap e.g. varying the particle-film spacing. If a less tightly confined electric field, thus a larger spacing, indeed leads to a linewidth broadening, this effect could be attributed to radiation damping.

- The measured linewidths of the longitudinal dipoles are much narrower than the simulated ones. This is could be due to the dielectric function of gold

49

that is used in the simulations. It would therefore be useful to measure the dielectric function of the gold films and of the gold nanoparticles. Furthermore, the presence of the chromium layer greatly influences the scattering spectra of gold nanoparticles on the 10 nm and 15 nm films. Lozanova et al. reported that the dielectric function of thin chromium films depends on the thickness of the layer. The dielectric function of metallic film can be calculated from the transmittance and reflectance spectra of the film [78]. Measurement on the dielectric function of single nanoparticles are performed by Stoller et al. where the complex polarizability and thereby the dielectric function is assessed of gold nanoparticles [79].

- In Chapter 6 it is concluded that for the 45 nm gold film exhibits the largest intensity changes at a probe wavelength for an increasing spacing, due to the narrow linewidth of the longitudinal dipole. This will therefore be the most suitable film thickness for the proposed biosensor. The scattering intensity is now only assessed at a probe wavelength of 700 nm. The intensity changes for varying spacer thicknesses could be assessed for different probe wavelengths in order to study if other probe wavelengths exhibit larger intensity changes. Experimentally, this could be studied by measuring the scattering intensity of nanoparticles on a 45 nm film at one wavelength using a band-pass filter. However, a lot of scattered light will be filter, such that long integration times ($\sim$10 s) are needed in order to collect enough light. A single wavelength light source will eliminate the need for filtering, such that shorter integration times can be used.

Appendices

Appendix A

Derivation electric dipole fields

The field of a dipole in a homogeneous, linear and isotropic space can be derived by considering two oscillating charges $\mathbf{q}$ of opposite sign, separated by an infinitesimal spacing $d\mathbf{s}$, and thus a dipole moment $\boldsymbol{\mu} = qd\mathbf{s}$. Assuming that all fields are induced by the dipole, gives an electric field

$$\mathbf{E}(\mathbf{r}) = \omega^2 \mu \mu_0 \overset{\leftrightarrow}{\mathbf{G}}(\mathbf{r}, \mathbf{r_0})\boldsymbol{\mu}, \tag{A.1}$$

where ω is the oscillation frequency, μ_0 is the vacuum permeability, μ is the permeability of the medium, the dipole is located at $\mathbf{r} = \mathbf{r_0}$ and the dyadic Green's function $\overset{\leftrightarrow}{\mathbf{G}}$, a second order tensor which is represented by a 3×3 matrix, where each column specifies the electric field of a dipole whose axis is aligned with one of the three coordinate axes. In a homogeneous space, $\overset{\leftrightarrow}{\mathbf{G}}$ is given by

$$\overset{\leftrightarrow}{\mathbf{G}}(\mathbf{r}, \mathbf{r_0}) = (\overset{\leftrightarrow}{\mathbf{I}} + \frac{1}{k^2}\nabla\nabla)G(\mathbf{r}, \mathbf{r_0}), \tag{A.2}$$

where $\overset{\leftrightarrow}{\mathbf{I}}$ is dyadic the unit tensor, k is the wave number and the scalar Green's function is given by

$$G(\mathbf{r}, \mathbf{r_0}) = \frac{\exp(ik|\mathbf{r} - \mathbf{r_0}|)}{4\pi|\mathbf{r} - \mathbf{r_0}|}. \tag{A.3}$$

From equations (A.2) and (A.3) it follows that in a Cartesian system

$$\overset{\leftrightarrow}{\mathbf{G}}(\mathbf{r}, \mathbf{r_0}) = \frac{\exp(ikR)}{4\pi R}\left[\left(1 + \frac{ikR - 1}{k^2R^2}\right)\overset{\leftrightarrow}{\mathbf{I}} + \frac{3 - 3ikR - k^2R^2}{k^2R^2}\frac{\mathbf{RR}}{R^2}\right], \tag{A.4}$$

where $R = |\mathbf{r} - \mathbf{r_0}|$ and $\mathbf{RR}$ denotes the outer product of $\mathbf{R}$ with itself. Three ranges can be distinguished in $\overset{\leftrightarrow}{\mathbf{G}}$: the near-field region where $R < \lambda$ and the $(kR)^{-2}$ terms dominate, the far field, R> 2λ, where only the $(kR)^0$ terms survive and the intermediate field where $\lambda <$R$< 2\lambda$ and $(kR)^{-1}$ terms dominate.

The Green's functions for these regions are then given by

$$\overset{\leftrightarrow}{\mathbf{G}}_{\mathbf{NF}} = \frac{\exp(ikR)}{4\pi R} \frac{1}{(kR)^2}(-\overset{\leftrightarrow}{\mathbf{I}} + 3\mathbf{R}\mathbf{R}/R^2), \tag{A.5}$$

$$\overset{\leftrightarrow}{\mathbf{G}}_{\mathbf{IF}} = \frac{\exp(ikR)}{4\pi R} \frac{i}{(kR)}(\overset{\leftrightarrow}{\mathbf{I}} - 3\mathbf{R}\mathbf{R}/R^2), \tag{A.6}$$

$$\overset{\leftrightarrow}{\mathbf{G}}_{\mathbf{FF}} = \frac{\exp(ikR)}{4\pi R}(\overset{\leftrightarrow}{\mathbf{I}} - \mathbf{R}\mathbf{R}/R^2), \tag{A.7}$$

where $\overset{\leftrightarrow}{\mathbf{G}}_{\mathbf{NF}}$, $\overset{\leftrightarrow}{\mathbf{G}}_{\mathbf{IF}}$, $\overset{\leftrightarrow}{\mathbf{G}}_{\mathbf{FF}}$ are the near-field, intermediate field and far-field Green's functions respectively.
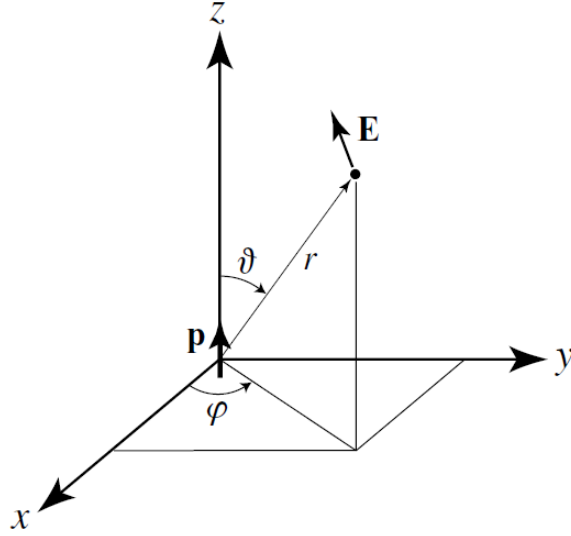

Figure A.1: The fields of a dipole are represented in a spherical coordinate system (r, θ, ϕ) in which the dipole points along the z-axis ($\theta = 0$).

Consider an origin at $\mathbf{r} = \mathbf{r_0}$ and a dipole orientation along the z-axis, $\boldsymbol{\mu} = |\boldsymbol{\mu}|\mathbf{n_z}$. The fields are now represented in spherical coordinates $\mathbf{r} = (r, \theta, \phi)$, Figure A.1, and $E = (E_r, E_\theta, E_\phi)$. Combining equations (A.1) (A.4) then gives

$$E_r = \frac{\boldsymbol{\mu}\cos(\theta)}{4\pi\varepsilon_0\varepsilon} \frac{\exp(ikr)}{r} k^2 \left(\frac{2}{k^2 r^2} - \frac{2i}{kr} \right), \tag{A.8}$$

$$E_\theta = \frac{\boldsymbol{\mu}\sin(\theta)}{4\pi\varepsilon_0\varepsilon} \frac{\exp(ikr)}{r} k^2 \left(\frac{1}{k^2 r^2} - \frac{i}{kr} - 1 \right), \tag{A.9}$$

$$E_\phi = 0. \tag{A.10}$$

E_r thus has no far-field term. The time dependent fields can be derived by substituting

$$\exp(ikr)k^m\boldsymbol{\mu} = \exp(ikr)\left(\frac{in}{c}\right)^m(-i\omega)^m\boldsymbol{\mu}, \tag{A.11}$$

which can be expressed in the time-domain by taking the Fourier transform:

$$\exp(ikr)k^m\boldsymbol{\mu} = \left(\frac{in}{c}\right)^m\frac{d^m}{dt^m}\boldsymbol{\mu}(t - nr/c), \tag{A.12}$$

and thus give the time-dependent fields:

$$E_r = \frac{\cos(\theta)}{4\pi\varepsilon_0\varepsilon}\left(\frac{2}{r^3} + \frac{n}{c}\frac{2}{r^2}\frac{d}{dt}\right)|\boldsymbol{\mu}(t - nr/c)|, \tag{A.13}$$

$$E_\theta = \frac{\sin(\theta)}{4\pi\varepsilon_0\varepsilon}\left(\frac{1}{r^3} + \frac{n}{c}\frac{1}{r^2} + \frac{n^2}{c^2}\frac{1}{r}\frac{d^2}{dt^2}\right)|\boldsymbol{\mu}(t - nr/c)|, \tag{A.14}$$

where n is the refractive index of the medium. The far-field is thus generated by the acceleration, the intermediate-field by the speed and the near-field by the position of the conducting electrons.

Appendix B

Gold film surface roughness

C

1.8 nm

-1.7 nm

0.0   50.0 μm
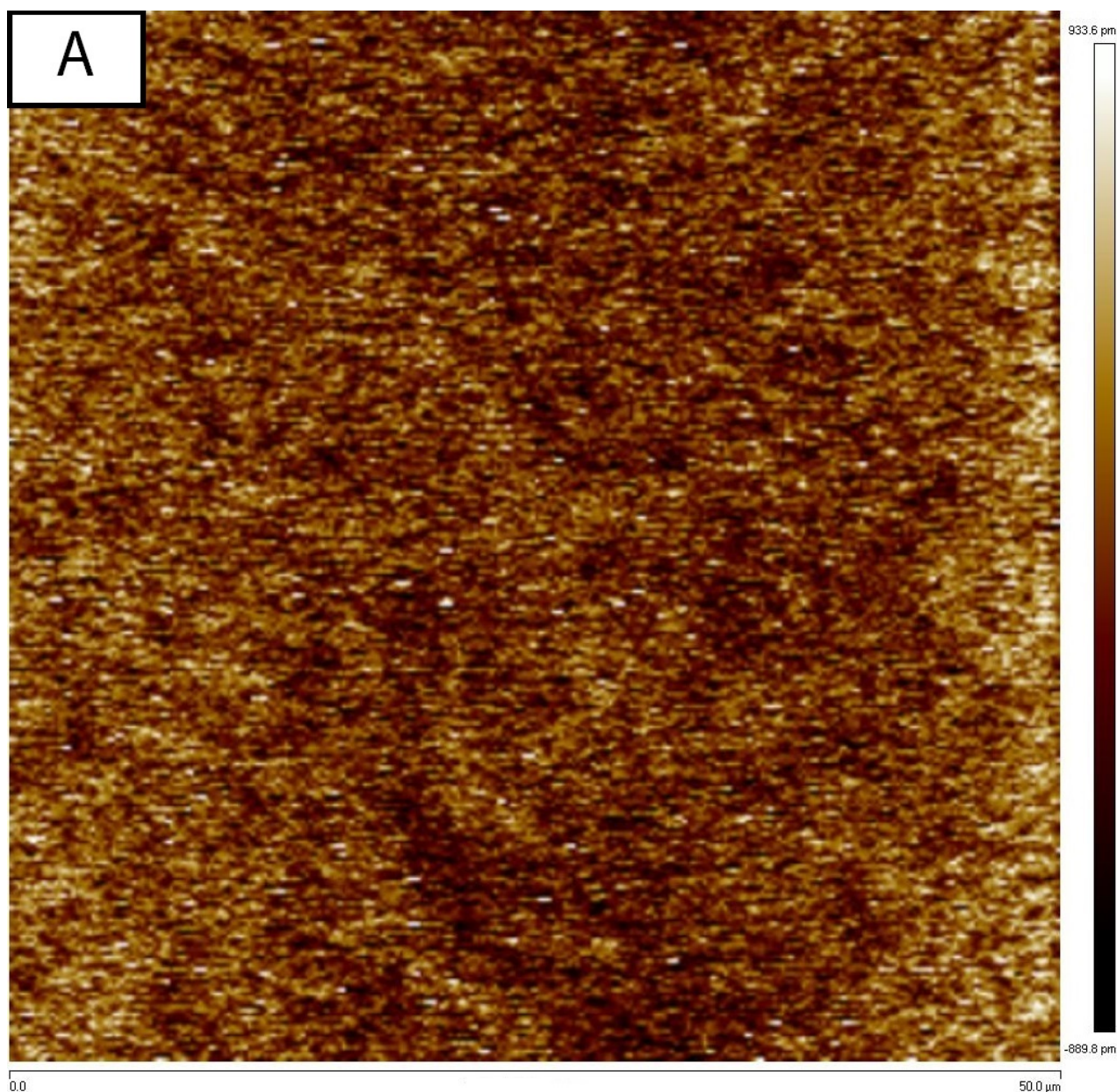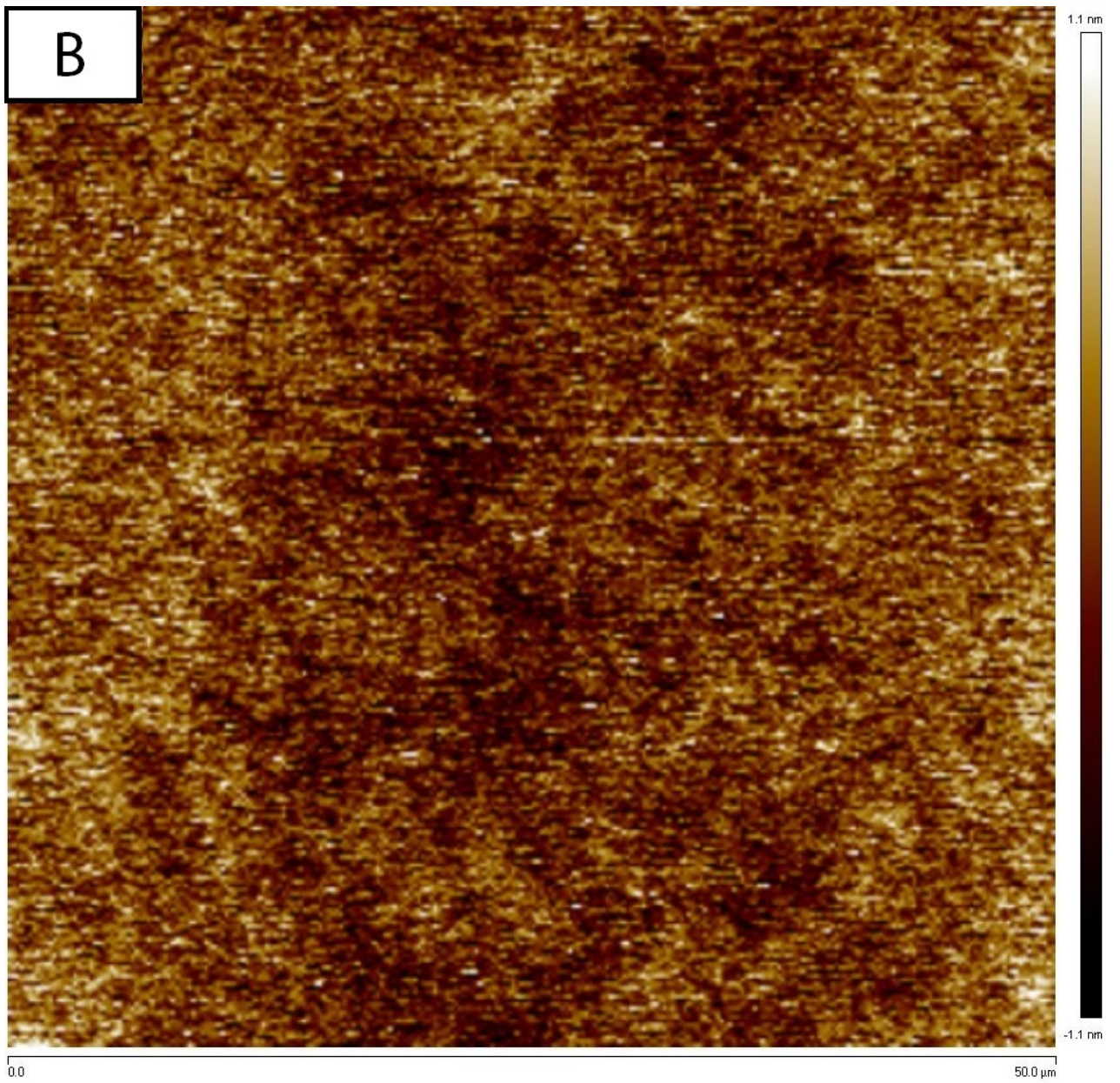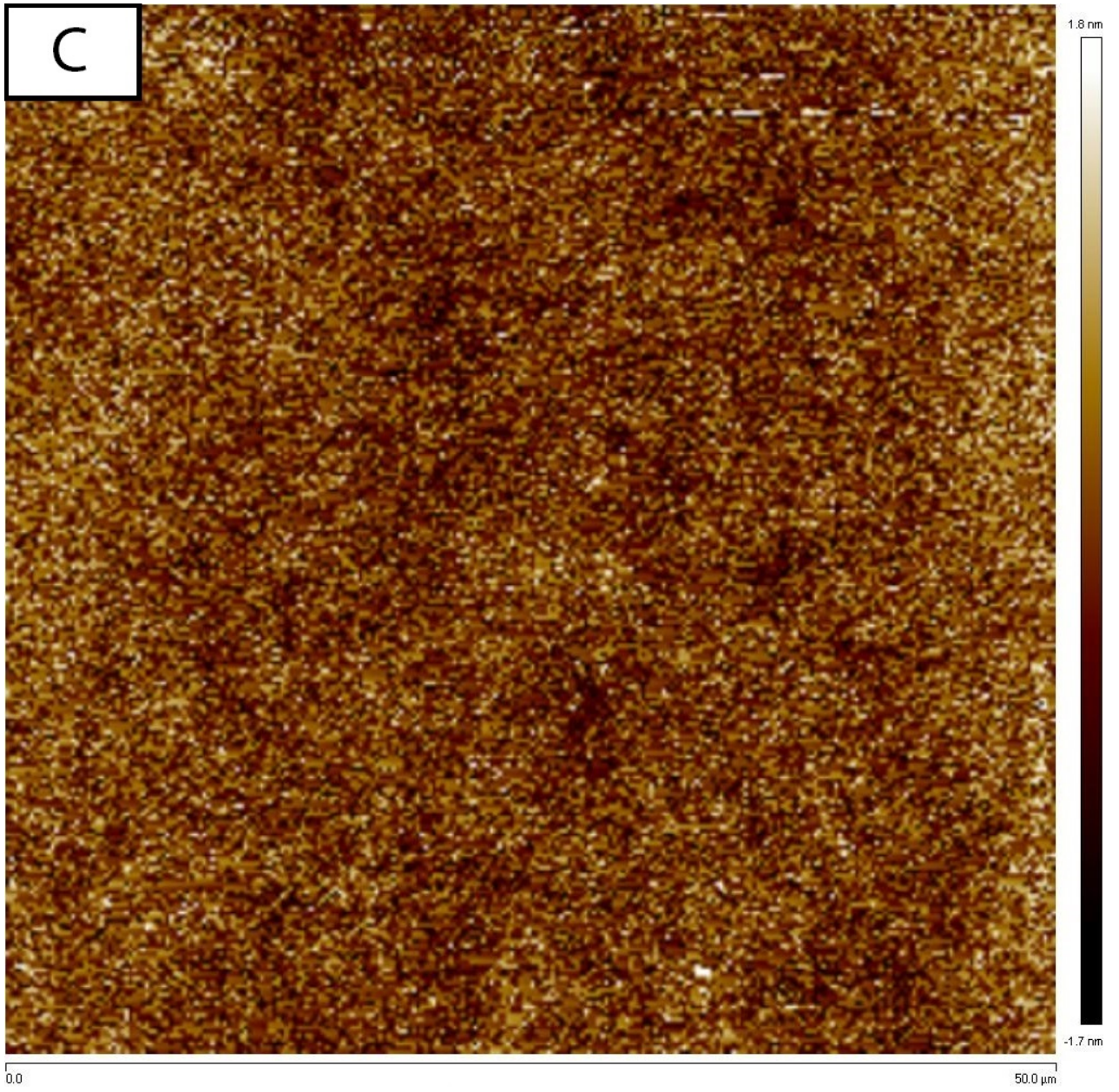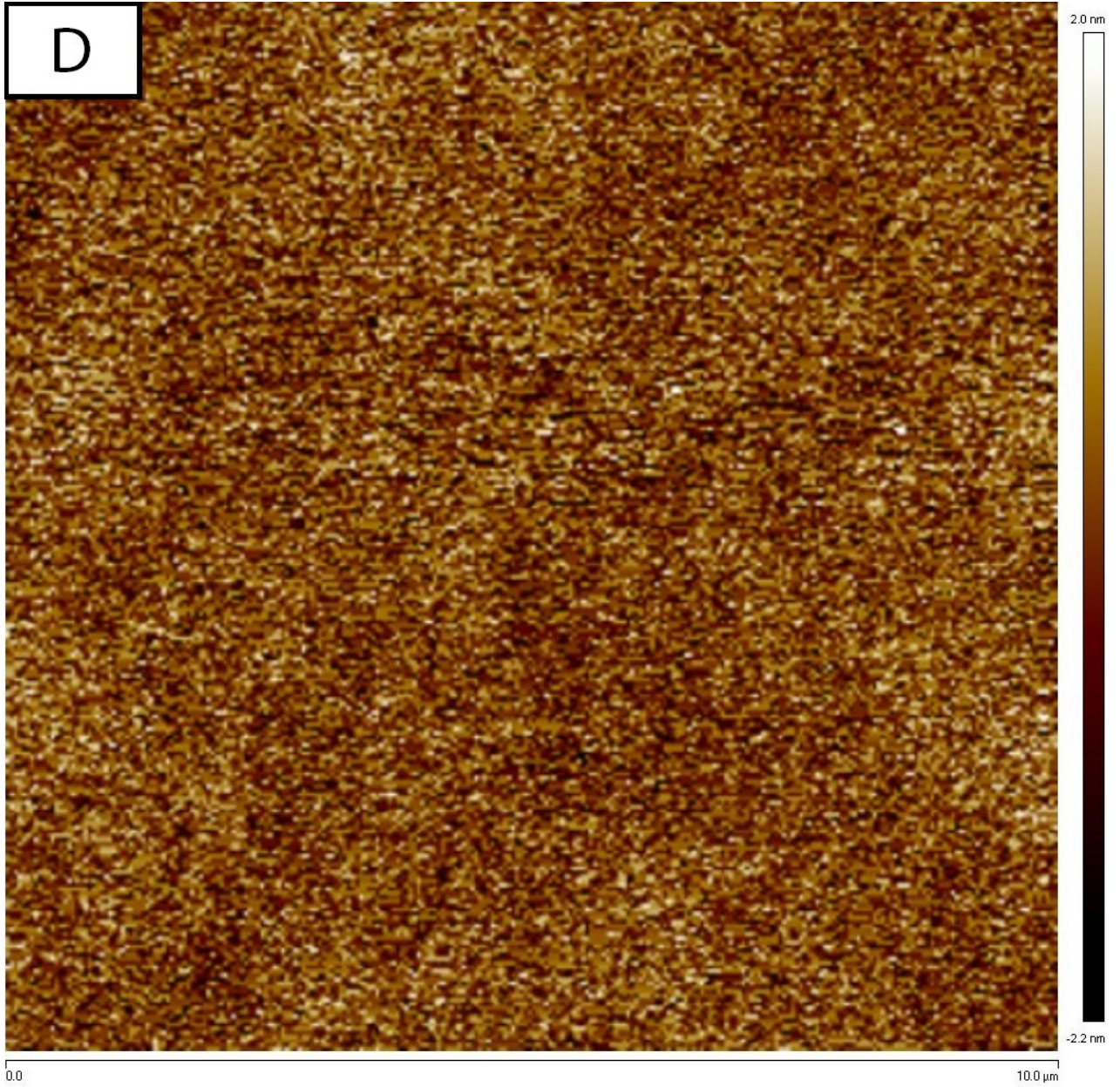
Figure B.1: (A-D) AFM height analysis images of a 10nm gold film (A), 15nm gold film (B), 30nm gold film (C), and 45 nm gold film (D). Note that the color bar scales vary slightly for each image. Surface roughness scan data(R_q and R_a)for multiple scans per sample are presented in Table B.1.

Table B.1: Values of R_q and R_a, measured using AFM on film thicknesses of 45nm, 30nm, 15nm and 10nm along 50μm lines.

| Film thickness (nm)	R_q(nm)	R_a(nm)
45	0.489	0.385
	0.559	0.388
	0.323	0.256
	0.378	0.27
30	0.484	0.385
	0.48	0.382
	0.484	0.385
	0.484	0.384
	0.324	0.257
	0.332	0.263
15	0.492	0.388
	0.461	0.363
	0.354	0.28
	0.294	0.231
	0.311	0.245
	0.293	0.23
	0.313	0.248
	0.282	0.221
	0.45	0.351
	0.439	0.344
	0.427	0.322
	0.426	0.323
10	0.243	0.191
	0.24	0.188
	1.14	0.367
	0.41	0.319
	0.248	0.194
	0.237	0.186
	0.584	0.415
	0.506	0.382

Appendix C

Gold film thickness
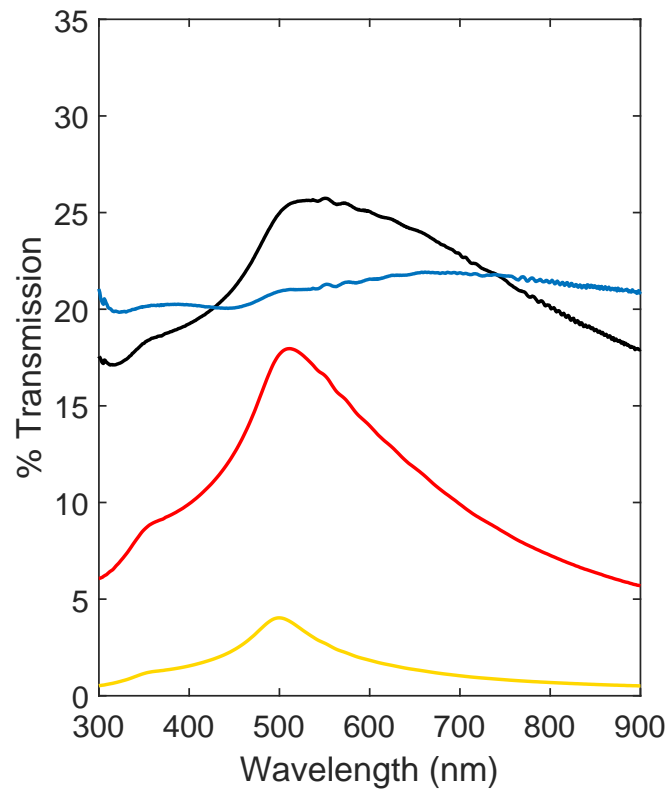
Figure C.1: UV-Vis spectroscopy measurements on the transmission of gold films with thicknesses of (blue) 10nm, (black) 15nm, (red) 30nm and (yellow) 45nm. The increasing film thickness leads to a lower transmission, with almost total extinction at 45nm, where the film acts as a near perfect mirror. Earlier studies have reported the large change in spectral profiles when thickening the film from 10 to 15nm [73, 80]. The presence of the 5nm chromium adhesion layer has a much stronger impact on the thinner (<30nm) films. This is reported to lead to a higher optical absorption from 300-400nm and a broadening of the gold absorption peak [80].

Bibliography

[1] Kenneth E Blick. Economics of point-of-care (poc) testing for cardiac markers and b-natriuretic peptide (bnp). *Point of Care*, 4(1):11–14, 2005.

[2] H Von Schenck, M Falkensson, and B Lundberg. Evaluation of" hemocue," a new device for determining hemoglobin. *Clinical chemistry*, 32(3):526–529, 1986.

[3] Myung-Hyun Nam, Kyoung Ho Roh, Hui-Nam Pak, Chang Kyu Lee, Young-Hoon Kim, Kap No Lee, and Yunjung Cho. Evaluation of the roche coaguchek xs handheld coagulation analyzer in a cardiac outpatient clinic. *Annals of Clinical & Laboratory Science*, 38(1):37–40, 2008.

[4] Joesph Wiencek and James Nichols. Issues in the practical implementation of poct: overcoming challenges. *Expert review of molecular diagnostics*, 16(4):415–422, 2016.

[5] Boris Roderick Roszek, Elisabeth Susanna Maria Hilbers-Modderman, G Doornbos, and AW van Drongelen. Point-of-care testen in de nederlandse ziekenhuizen: Borging van kwaliteit en veiligheid. 2013.

[6] Xiaowei Guo. Surface plasmon resonance based biosensor technique: a review. *Journal of biophotonics*, 5(7):483–501, 2012.

[7] Jeffrey I Joseph, Brian Hipszer, Boris Mraovic, Inna Chervoneva, Mark Joseph, and Zvi Grunwald. Clinical need for continuous glucose monitoring in the hospital, 2009.

[8] Moritoki Egi, Rinaldo Bellomo, Edward Stachowski, Craig J French, and Graeme Hart. Variability of blood glucose concentration and short-term mortality in critically ill patients. *Anesthesiology: The Journal of the American Society of Anesthesiologists*, 105(2):244–252, 2006.

[9] Karine Bagramyan, Jason R Barash, Stephen S Arnon, and Markus Kalkum. Attomolar detection of botulinum toxin type a in complex biological matrices. *PloS one*, 3(4):e2041, 2008.

[10] Haitao Li, Liming Ying, Jeremy J Green, Shankar Balasubramanian, and David Klenerman. Ultrasensitive coincidence fluorescence detection of single dna molecules. *Analytical chemistry*, 75(7):1664–1670, 2003.

[11] Michael J Schoning and Arshak Poghossian. Label-free biosensing.

[12] Adam B Taylor and Peter Zijlstra. Single-molecule plasmon sensing: current status and future prospects. *ACS sensors*, 2(8):1103–1122, 2017.

[13] S Coyle, MC Netti, JJ Baumberg, MA Ghanem, PR Birkin, PN Bartlett, and DM Whittaker. Confined plasmons in metallic nanocavities. *Physical review letters*, 87(17):176801, 2001.

[14] Stefan Enoch, Romain Quidant, and Gonçal Badenes. Optical sensing based on plasmon coupling in nanoparticle arrays. *Optics express*, 12(15):3422–3427, 2004.

[15] Amanda J Haes and Richard P Van Duyne. A nanoscale optical biosensor: sensitivity and selectivity of an approach based on the localized surface plasmon resonance spectroscopy of triangular silver nanoparticles. *Journal of the American Chemical Society*, 124(35):10596–10604, 2002.

[16] Prashant K Jain, Xiaohua Huang, Ivan H El-Sayed, and Mostafa A El-Sayed. Noble metals on the nanoscale: optical and photothermal properties and some applications in imaging, sensing, biology, and medicine. *Accounts of chemical research*, 41(12):1578–1586, 2008.

[17] Peter Zijlstra, Pedro MR Paulo, and Michel Orrit. Optical detection of single non-absorbing molecules using the surface plasmon resonance of a gold nanorod. *Nature nanotechnology*, 7(6):379, 2012.

[18] Michael A Beuwer, Menno WJ Prins, and Peter Zijlstra. Stochastic protein interactions monitored by hundreds of single-molecule plasmonic biosensors. *Nano letters*, 15(5):3507–3511, 2015.

[19] Irene Ament, Janak Prasad, Andreas Henkel, Sebastian Schmachtel, and Carsten Sönnichsen. Single unlabeled protein detection on individual plasmonic nanoparticles. *Nano letters*, 12(2):1092–1095, 2012.

[20] G. J. Nusz, S. M. Marinakos, A. C. Curry, A. Dahlin, F. Hook, A. Wax, and A. Chilkoti. Label-free plasmonic detection of biomolecular binding by a single gold nanorod. *Analytical Chemistry*, 80(4):984–989, 2008.

[21] Karina R Seferian, Natalia N Tamm, Alexander G Semenov, Anastasia A Tolstaya, Ekaterina V Koshkina, Mihail I Krasnoselsky, Alexander B Postnikov, Daria V Serebryanaya, Fred S Apple, MaryAnn M Murakami, et al. Immunodetection of glycosylated nt-probnp circulating in human blood. *Clinical chemistry*, 54(5):866–873, 2008.

[22] Kazuo Uchida and Akiko Gotoh. Measurement of cystatin-c and creatinine in urine. *Clinica chimica acta*, 323(1-2):121–128, 2002.

[23] PJ Hunt, AM Richards, MG Nicholls, TG Yandle, RN Doughty, and EA Espiner. Immunoreactive amino-terminal pro-brain natriuretic peptide (nt-probnp): a new marker of cardiac impairment. *Clinical endocrinology*, 47(3):287–296, 1997.

[24] Christos Angelidis, Spyridon Deftereos, Georgios Giannopoulos, Nikolaos Anatoliotakis, Georgios Bouras, Georgios Hatzis, Vasiliki Panagopoulou, Vlasios Pyr-

gakis, and Michael W Cleman. Cystatin c: an emerging biomarker in cardiovascular disease. *Current topics in medicinal chemistry*, 13(2):164–179, 2013.

[25] Sachin S Soni, Dinna Cruz, Ilona Bobek, Chang Yin Chionh, Federico Nalesso, Paolo Lentini, Massimo de Cal, Valentina Corradi, Grazia Virzi, and Claudio Ronco. Ngal: a biomarker of acute kidney injury and other systemic conditions. *International urology and nephrology*, 42(1):141–150, 2010.

[26] Emiel WA Visser, Matej Horacek, and Peter Zijlstra. Plasmon rulers as a probe for real-time microsecond conformational dynamics of single molecules. *Nano letters*, 18(12):7927–7934, 2018.

[27] Q Zhang, GC Li, TW Lo, and DY Lei. Polarization-resolved optical response of plasmonic particle-on-film nanocavities. *Journal of Optics*, 20(2):024010, 2018.

[28] M Valenti, MP Jonsson, G Biskos, A Schmidt-Ott, and WA Smith. Plasmonic nanoparticle-semiconductor composites for efficient solar water splitting. *Journal of Materials Chemistry A*, 4(46):17891–17912, 2016.

[29] Jack J Mock, Ryan T Hill, Aloyse Degiron, Stefan Zauscher, Ashutosh Chilkoti, and David R Smith. Distance-dependent plasmon resonant coupling between a gold nanoparticle and gold film. *Nano letters*, 8(8):2245–2252, 2008.

[30] Cristian Ciracì, Xiaoshu Chen, Jack J Mock, Felicia McGuire, Xiaojun Liu, Sang-Hyun Oh, and David R Smith. Film-coupled nanoparticles by atomic layer deposition: Comparison with organic spacing layers. *Applied Physics Letters*, 104(2):023109, 2014.

[31] Charlie Readman, Bart de Nijs, Istvan Szabo, Angela Demetriadou, Ryan D Greenhalgh, Colm Durkan, Edina Rosta, Oren Scherman, and Jeremy J Baumberg. Anomalously large spectral shifts near the quantum tunnelling limit in plasmonic rulers with subatomic resolution. *Nano letters*, 2019.

[32] Marie-Elena Kleemann, Jan Mertens, Xuezhi Zheng, Sean Cormier, Vladimir Turek, Felix Benz, Rohit Chikkaraddy, William Deacon, Anna Lombardi, Victor V Moshchalkov, et al. Revealing nanostructures through plasmon polarimetry. *ACS nano*, 11(1):850–855, 2016.

[33] Christopher J Orendorff, Anand Gole, Tapan K Sau, and Catherine J Murphy. Surface-enhanced raman spectroscopy of self-assembled monolayers: sandwich architecture and nanoparticle shape dependence. *Analytical chemistry*, 77(10): 3261–3266, 2005.

[34] Jeremy J Baumberg, Javier Aizpurua, Maiken H Mikkelsen, and David R Smith. Extreme nanophotonics from ultrathin metallic gaps. *Nature materials*, page 1, 2019.

[35] Tao Wang and Christian A Nijhuis. Molecular electronic plasmonics. *Applied Materials Today*, 3:73–86, 2016.

[36] Tanya Hutter, Fu Min Huang, Stephen R Elliott, and Sumeet Mahajan. Near-field plasmonics of an individual dielectric nanoparticle above a metallic substrate. *The Journal of Physical Chemistry C*, 117(15):7784–7790, 2013.

[37] Huanjun Chen, Tian Ming, Shouren Zhang, Zhao Jin, Baocheng Yang, and Jianfang Wang. Effect of the dielectric properties of substrates on the scattering patterns of gold nanorods. *Acs Nano*, 5(6):4865–4877, 2011.

[38] Akira Yamaguchi, Saulius Juodkazis, Shigeki Matsuo, and Hiroaki Misawa. Enhancement of surface plasmon resonance sensing for dna hybridization using colloidal au attached probe dna. *Chemistry letters*, 31(2):190–191, 2002.

[39] Zixuan Chen, Yujiao Peng, Yue Cao, Hui Wang, Jian-Rong Zhang, Hong-Yuan Chen, and Jun-Jie Zhu. Light-driven nano-oscillators for label-free single-molecule monitoring of microrna. *Nano letters*, 18(6):3759–3765, 2018.

[40] Lehui Lu, Guoying Sun, Hongjie Zhang, Haishui Wang, Shiquan Xi, Jianqiang Hu, Zhongqun Tian, and Ray Chen. Fabrication of core-shell au-pt nanoparticle film and its potential application as catalysis and sers substrate. *Journal of materials chemistry*, 14(6):1005–1009, 2004.

[41] Bo Yan, Anupama Thubagere, W Ranjith Premasiri, Lawrence D Ziegler, Luca Dal Negro, and Bjorn M Reinhard. Engineered sers substrates with multiscale signal enhancement: nanoparticle cluster arrays. *Acs Nano*, 3(5):1190–1202, 2009.

[42] Charles Kittel et al. *Introduction to solid state physics*, volume 8. Wiley New York, 1976.

[43] David Bohm and Eugene P Gross. Theory of plasma oscillations. a. origin of medium-like behavior. *Physical Review*, 75(12):1851, 1949.

[44] Lukas Novotny and Bert Hecht. *Principles of nano-optics*. Cambridge university press, 2012.

[45] Peter B Johnson and R-W₋ Christy. Optical constants of the noble metals. *Physical review B*, 6(12):4370, 1972.

[46] Edward D Palik. *Handbook of optical constants of solids*, volume 3. Academic press, 1998.

[47] Jiřı Homola, Sinclair S Yee, and Günter Gauglitz. Surface plasmon resonance sensors. *Sensors and Actuators B: Chemical*, 54(1-2):3–15, 1999.

[48] Stefan A Maier and Harry A Atwater. Plasmonics: Localization and guiding of electromagnetic energy in metal/dielectric structures. *Journal of applied physics*, 98(1):10, 2005.

[49] Miguel A García. Surface plasmons in metallic nanoparticles: fundamentals and applications. *Journal of Physics D: Applied Physics*, 44(28):283001, 2011.

[50] Stefan Alexander Maier. *Plasmonics: fundamentals and applications*. Springer Science & Business Media, 2007.

[51] Armen Melikyan and Hayk Minassian. On surface plasmon damping in metallic nanoparticles. *Applied Physics B*, 78(3-4):453–455, 2004.

[52] Daniel Gall. Electron mean free path in elemental metals. *Journal of Applied Physics*, 119(8):085101, 2016.

[53] H Baida, Pierre Billaud, S Marhaba, D Christofilos, Emmanuel Cottancin, Aurelien Crut, Jean Lerme, Paolo Maioli, Michel Pellarin, Michel Broyer, et al. Quantitative determination of the size dependence of surface plasmon resonance damping in single ag@ sio2 nanoparticles. *Nano letters*, 9(10):3463–3469, 2009.

[54] Warren L Stutzman and Gary A Thiele. *Antenna theory and design*. John Wiley & Sons, 2012.

[55] Jörg P Kottmann, Olivier JF Martin, David R Smith, and Sheldon Schultz. Dramatic localized electromagnetic enhancement in plasmon resonant nanowires. *Chemical Physics Letters*, 341(1-2):1–6, 2001.

[56] Encai Hao and George C Schatz. Electromagnetic fields around silver nanoparticles and dimers. *The Journal of chemical physics*, 120(1):357–366, 2004.

[57] P Nordlander and F Le. Plasmonic structure and electromagnetic field enhancements in the metallic nanoparticle-film system. *Applied Physics B*, 84(1-2):35, 2006.

[58] Hayden K Webb, Vi Khanh Truong, Jafar Hasan, Christopher Fluke, Russell J Crawford, and Elena P Ivanova. Roughness parameters for standard description of surface nanoarchitecture. *Scanning*, 34(4):257–263, 2012.

[59] FJ Garcia De Abajo and A Howie. Retarded field calculation of electron energy loss in inhomogeneous dielectrics. *Physical Review B*, 65(11):115418, 2002.

[60] Ulrich Hohenester and Andreas Trügler. Mnpbem–a matlab toolbox for the simulation of plasmonic nanoparticles. *Computer Physics Communications*, 183 (2):370–381, 2012.

[61] Ulrich Hohenester. Simulating electron energy loss spectroscopy with the mnpbem toolbox. *Computer Physics Communications*, 185(3):1177–1187, 2014.

[62] Jürgen Waxenegger, Andreas Trügler, and Ulrich Hohenester. Plasmonics simulations with the mnpbem toolbox: Consideration of substrates and layer structures. *Computer Physics Communications*, 193:138–150, 2015.

[63] Lulu Han, Zhengwei Mao, He Wuliyasu, Jindan Wu, Xiao Gong, Yuguang Yang, and Changyou Gao. Modulating the structure and properties of poly (sodium 4-styrenesulfonate)/poly (diallyldimethylammonium chloride) multilayers with concentrated salt solutions. *Langmuir*, 28(1):193–199, 2011.

[64] Christopher P Burrows and William L Barnes. Large spectral extinction due to overlap of dipolar and quadrupolar plasmonic modes of metallic nanoparticles in arrays. *Optics express*, 18(3):3187–3198, 2010.

[65] Jorge Zuloaga, Emil Prodan, and Peter Nordlander. Quantum description of the plasmon resonances of a nanoparticle dimer. *Nano letters*, 9(2):887–891, 2009.

[66] C Ciracì, RT Hill, JJ Mock, Y Urzhumov, AI Fernández-Domínguez, SA Maier,

JB Pendry, A Chilkoti, and DR Smith. Probing the ultimate limits of plasmonic enhancement. *Science*, 337(6098):1072–1074, 2012.

[67] W Rechberger, A Hohenau, A Leitner, JR Krenn, B Lamprecht, and FR Aussenegg. Optical properties of two interacting gold nanoparticles. *Optics communications*, 220(1-3):137–141, 2003.

[68] Rui Qiang, Richard L Chen, and Ji Chen. Modeling electrical properties of gold films at infrared frequency using fdtd method. *International journal of infrared and millimeter waves*, 25(8):1263–1270, 2004.

[69] F Le, NZ Lwin, JM Steele, Mikael Käll, NJ Halas, and P Nordlander. Plasmons in the metallic nanoparticle- film system as a tunable impurity problem. *Nano Letters*, 5(10):2009–2013, 2005.

[70] Chatdanai Lumdee, Binfeng Yun, and Pieter G Kik. Effect of surface roughness on substrate-tuned gold nanoparticle gap plasmon resonances. *Nanoscale*, 7(9): 4250–4255, 2015.

[71] Ali Sobhani, Alejandro Manjavacas, Yang Cao, Michael J McClain, F Javier Garcia de Abajo, Peter Nordlander, and Naomi J Halas. Pronounced linewidth narrowing of an aluminum nanoparticle plasmon resonance by interaction with an aluminum metallic film. *Nano letters*, 15(10):6946–6951, 2015.

[72] Robert L Olmon, Brian Slovick, Timothy W Johnson, David Shelton, Sang-Hyun Oh, Glenn D Boreman, and Markus B Raschke. Optical dielectric function of gold. *Physical Review B*, 86(23):235147, 2012.

[73] V Lozanova, A Lalova, L Soserov, and R Todorov. Optical and electrical properties of very thin chromium films for optoelectronic devices. In *Journal of Physics: Conference Series*, volume 514, page 012003. IOP Publishing, 2014.

[74] Eduardo Guzmán, Hernán Ritacco, José EF Rubio, Ramón G Rubio, and Francisco Ortega. Salt-induced changes in the growth of polyelectrolyte layers of poly (diallyl-dimethylammonium chloride) and poly (4-styrene sulfonate of sodium). *Soft Matter*, 5(10):2130–2142, 2009.

[75] James T Hugall, Anshuman Singh, and Niek F van Hulst. Plasmonic cavity coupling. *Acs Photonics*, 5(1):43–53, 2018.

[76] JA Dionne, A Baldi, B Baum, C-S Ho, V Janković, GV Naik, T Narayan, JA Scholl, and Yang Zhao. Localized fields, global impact: Industrial applications of resonant plasmonic materials. *Mrs Bulletin*, 40(12):1138–1145, 2015.

[77] JW Elam, ZA Sechrist, and SM George. Zno/al2o3 nanolaminates fabricated by atomic layer deposition: growth and surface roughness measurements. *Thin Solid Films*, 414(1):43–55, 2002.

[78] R Todorov, A Lalova, K Petkov, and J Tasseva. Spectral properties of the silver photodoping process in thin as–s–se layers. *Semiconductor Science and Technology*, 27(11):115014, 2012.

[79] Patrick Stoller, Volker Jacobsen, and Vahid Sandoghdar. Measurement of the complex dielectric constant of a single gold nanoparticle. *Optics letters*, 31(16): 2474–2476, 2006.

[80] Jakub Siegel, Olexiy Lyutakov, Vladimír Rybka, Zdeňka Kolská, and Václav Švorčík. Properties of gold nanostructures sputtered on glass. *Nanoscale research letters*, 6(1):96, 2011.